Economic Geology
Vol. 96, 2001, pp. 743–772

Porphyry-Epithermal Transition: Maricunga Belt, Northern Chile

JOHN L. MUNTEAN[†,*] AND MARCO T. EINAUDI

Department of Geological and Environmental Sciences, Stanford University, Stanford, California 94305-2115

Abstract

The Refugio, Aldebarán, and La Pepa districts in the Maricunga belt of northern Chile contain advanced argillic alteration zones that locally host high-sulfidation epithermal gold deposits in proximity to porphyry gold (± copper) deposits. The spatial association suggests a genetic link. Mineralized zones are characterized by four main vein types that formed at different times and have specific zonal relationships.

A-veinlets are the earliest and deepest vein type. They are restricted to potassic alteration zones in intrusive rocks. A-veinlets contain variable amounts of quartz, magnetite, biotite, and chalcopyrite and locally have K feldspar halos. They have nonmatching, irregular vein walls and lack internal symmetry. Hypersaline liquid-rich inclusions coexisting with vapor-rich inclusions in A-veinlets indicate temperatures as high as nearly 700°C and pressures between 200 and 400 bars. Assuming a lithostatic load, depths of 0.8 to 1.6 km are inferred. Zones of abundant A-veinlets contain mostly <1 ppm gold and 0.1 to 0.4 percent hypogene copper.

Banded quartz veinlets occur mostly above A-veinlets and cut A-veinlets where they overlap. Dark gray bands, the color resulting from a high density of vapor-rich fluid inclusions and micron-sized grains of magnetite, commonly occur as symmetric pairs near the vein walls. Vein walls are parallel and slightly wavy, vuggy vein centers are common, and alteration envelopes are absent. Data from rare liquid-rich inclusions in banded quartz veinlets indicate temperatures ≤350°C at pressures between 20 and 150 bars. Assuming a hydrostatic load, depths of 0.2 to 1.5 km are inferred. Zones of abundant banded quartz veinlets generally contain 0.5 to 2 ppm gold and <0.1 percent hypogene copper.

D-veins are pyrite veins with quartz-sericite-pyrite halos. They are widespread and crosscut A-veinlets and banded quartz veinlets. The brittle nature of D-veins and limited fluid inclusion data suggest temperatures <400°C. D-veins serve as important time lines. They are nowhere truncated or crosscut by intrusions, A-veinlets, or banded quartz veinlets.

Quartz-alunite replacement veins, referred to as ledges in this paper, are typical of the high-sulfidation epithermal environment. They are mostly limited to overlying volcanic rocks. They contain local core zones of vuggy residual quartz that can contain enargite or, at higher elevations, barite. Of the three districts studied only La Pepa has mineable quartz-alunite ledges, which contain an average gold grade of about 20 ppm.

A spectrum of porphyry-style deposits exists. Cerro Casale at Aldebarán shares many characteristics of porphyry copper deposits worldwide, whereas Verde at Refugio is a true porphyry gold deposit. Potassic alteration zones and A-veinlets are strongly developed at Cerro Casale, whereas they are absent at Verde. Banded quartz veinlets predominate at Verde, whereas they occur only at the upper levels of Cerro Casale. The Pancho deposit at Refugio and the Cavancha deposit at La Pepa are telescoped systems in which banded quartz veinlets overprint potassic alteration zones and A-veinlets.

A-veinlets and banded quartz veinlets cut and are cut by intrusions, indicating multiple cycles of intrusion→potassic alteration→A-veinlets→banded quartz veinlets during formation of porphyry-style mineralization. Banded quartz veinlets are thought to have formed by flashing of magmatic fluids during episodic transitions from lithostatic to hydrostatic pressure. Loss of sulfur to the vapor phase during flashing inhibited formation of copper-sulfides in banded quartz veinlets and, therefore, resulted in high gold/copper ratios. Where rising magmatic vapors condensed into overlying meteoric water along faults, barren quartz-alunite ledges formed. This conclusion is supported by equivalent $^{40}Ar/^{39}Ar$ dates on hydrothermal biotite associated with porphyry-style ore and alunite from barren ledges at Aldebarán.

$^{40}Ar/^{39}Ar$ dates at La Pepa indicate alunite formed at least 140,000 years to as long as 900,000 years after hydrothermal biotite. Within the high-sulfidation epithermal environment, the development of ore depends on the ability of late, moderate-salinity magmatic fluids to reach the surface without condensing a brine upon ascent. Cooling and boiling of the moderate-salinity fluid below its critical temperature results in the formation of sericite at depth and alunite near the surface that is essentially synchronous with high-sulfidation ore formation. The timing of the switch from lithostatic pressures to brittle hydrostatic conditions, relative to the life of the hydrothermal system, might determine how much porphyry-style ore forms relative to high-sulfidation epithermal ore.

Introduction

SPATIAL and temporal transitions within porphyry copper systems from potassic and intermediate sulfidation-state assemblages to advanced argillic and high sulfidation-state assemblages are relatively well established (Taylor, 1935; Meyer et al., 1968; Gustafson and Hunt, 1975; Einaudi, 1977, 1982; Brimhall, 1979). Transitions between porphyry copper deposits and high-sulfidation epithermal gold deposits also have been proposed (Sillitoe, 1973, 1983, 1988, 1989; Wallace, 1979; Heald et al., 1987; Rye, 1993), and recent studies of the Lepanto high-sulfidation gold-copper and adjacent Far Southeast porphyry copper-gold deposits (Arribas et al., 1995, Hedenquist

[†]Corresponding author: e-mail, JLMuntean@aol.com
[*]Present address: Placer Dome Exploration Inc, 240 S. Rock Blvd., Suite 117, Reno, Nevada 89502.

et al. 1998) have substantiated that such links do exist. As a further test of this link, we investigated the Maricunga belt of northern Chile, where numerous districts have zones of advanced argillic assemblages that locally host high-sulfidation epithermal gold deposits close to porphyry gold deposits (Vila and Sillitoe, 1991). This study focuses on the spatial and temporal relationships between the porphyry and epithermal styles of mineralization in three districts: Refugio, Aldebarán, and La Pepa. An additional goal of this study is to characterize the porphyry gold deposits in these three districts and underscore the differences between these and gold-rich porphyry copper deposits.

Geology of the Maricunga Belt

The Maricunga belt, located in northern Chile about 700 km north of Santiago (Figs. 1, 2), is a metallogenic province of Miocene age that contains numerous gold, silver, and copper deposits of porphyry and epithermal character (Vila and Sillitoe, 1991). The geology of the belt is known from the work of Segerstrom (1968), Zentilli (1974), Mercado (1982), Davidson and Mpodozis (1991), and Mpodozis et al. (1995). Pennsylvanian to Triassic granitoids and intermediate to silicic volcanic rocks are overlain by Mesozoic to early Tertiary

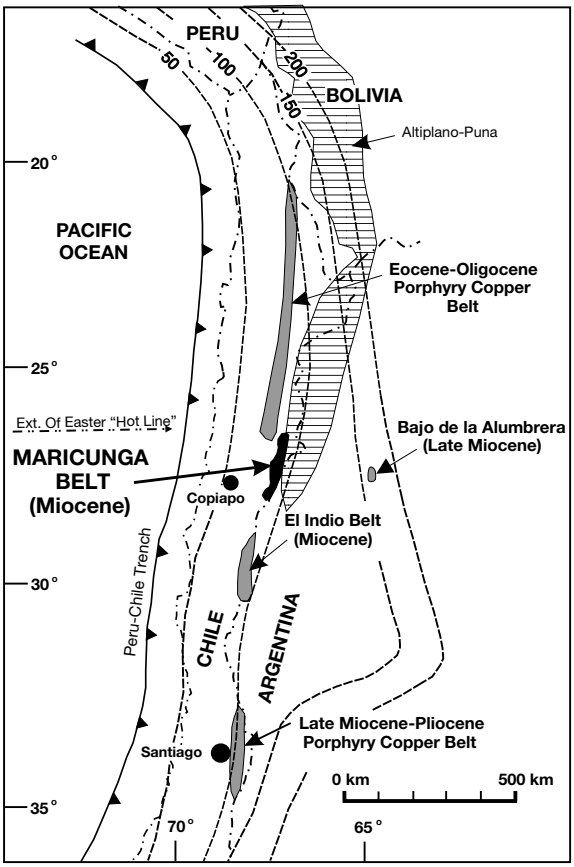

FIG. 1. Map showing the location of the Maricunga belt relative to other regional zones of important copper-gold mineralization in Chile and Argentina. Also shown are the Altiplano-Puna and the extension of the Easter "hot line" (cf. Bonnati et al., 1977). The contour lines represent depths in kilometers to the Benioff zone. Modified from Davidson and Mpodozis (1991).

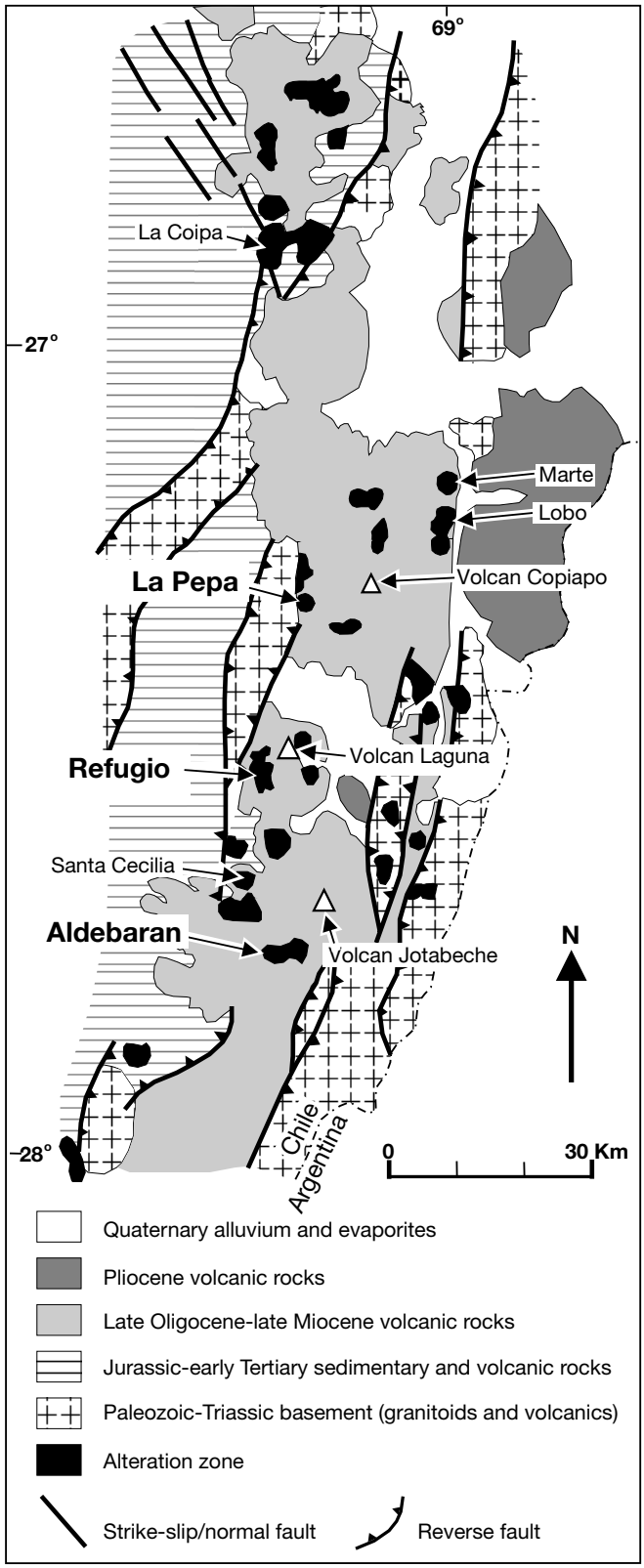

FIG. 2. Schematic geologic map of the Maricunga belt, modified from Davidson and Mpodozis (1991).

continental volcanic and clastic rocks. A north-northeast–trending chain of andesitic to dacitic composite volcanoes, part of a Miocene continental margin volcanoplutonic arc, defines the Maricunga belt. The belt lies in the transition zone to the northern boundary of the modern nonvolcanic, flat-slab region of the Chilean Andes (28°–33°S, Fig. 1). Flattening began in the middle Miocene (18 Ma) and resulted in basement uplift with blocks bounded by northeast-trending reverse faults and an eastward shift in volcanism in the late Miocene to early Pliocene (Jordan et al., 1983; Isacks, 1988; Allmendinger et al., 1990; Kay et al., 1991, 1994; Walker et al., 1991).

Erosion of Miocene volcanoes has exposed subvolcanic porphyry stocks, many of which are hydrothermally altered (Vila and Sillitoe, 1991). Several of the alteration zones host high-sulfidation gold-(silver) epithermal and porphyry gold-(copper) deposits. The high-sulfidation epithermal deposits, mostly hosted by volcanic rocks, include large-tonnage low-grade deposits (e.g., La Coipa; Oviedo et al., 1991) and bonanza-type veins (e.g., La Pepa). The porphyry gold-(copper) deposits (e.g., Refugio, Aldebarán, La Pepa, Marte, and Lobo) are associated with quartz veinlets hosted mainly by subvolcanic porphyry intrusions. Since 1980, an aggregate geologic resource of approximately 40 million ounces of gold has been discovered in the Maricunga belt.

Descriptions of Vein Types

Because hydrothermal processes in the three studied districts are deduced largely from the time-space distribution of different vein types, and because the three districts share common vein types, we start with a description of veins. The dominant vein types recognized at Refugio, Aldebarán, and La Pepa are classified by structure, texture, and to a lesser degree mineralogy, into the following groups (Table 1): A-veinlets (cf. Gustafson and Hunt, 1975), banded quartz veinlets (Vila and Sillitoe, 1991; Vila et al., 1991; King, 1992; Muntean and Einaudi, 2000), D-veins (cf. Gustafson and Hunt, 1975), and quartz-alunite ledges (cf. Ransome, 1909). The term ledge is used to refer to steeply dipping replacement veins.

Vila and Sillitoe (1991) and Vila et al. (1991) described quartz veinlets in the Maricunga porphyry gold deposits as interbanded translucent, white, gray, and black varieties of quartz. We equate these with the banded quartz veinlets described by Muntean and Einaudi (2000) at Refugio, but we make the distinction between these banded veinlets and earlier, granular quartz veinlets that correspond to A-veinlets commonly seen in porphyry copper and copper-gold deposits (e.g., Gustafson and Hunt, 1975; Clode et al., 1999). Table 1 summarizes the characteristics of veins in the three districts.

A-veinlets

The earliest vein type seen in the porphyry gold deposits at Refugio, Aldebarán, and La Pepa are A-veinlets, consisting of quartz-magnetite-biotite-chalcopyrite with variable contents of K feldspar, pyrite, and other minerals (Table 1). A-veinlets range in thickness from <0.2 mm to about 1 cm and are found only in intrusive rocks in pervasive potassic alteration zones. Vein quartz has a characteristic vitreous luster and anhedral granular texture that typically results in a sugary appearance. Lack of internal symmetry and nonmatching but sharply defined walls (Fig. 3) are characteristic and, except for local sulfide centerlines, evidence for open-space filling is absent. It is likely that A-veinlets formed at least in part by replacement of wall rock. Discontinuous A-veinlets (lengths less than a few centimeters) commonly are bordered by K feldspar halos, whereas continuous A-veinlets (lengths greater than tens of centimeters) commonly lack alteration envelopes. Both discontinuous and continuous varieties are locally truncated by intrusions that are subsequently cut by younger sets of A-veinlets. Although continuous varieties commonly cut and offset discontinuous varieties, the reverse relationship has been observed, suggesting multiple cycles of the sequence intrusion, potassic alteration, discontinuous A-veinlets, continuous A-veinlets (cf. Gustafson and Hunt, 1975).

Quartz in A-veinlets contains abundant fluid inclusions, 25 to 75 percent of which are liquid-rich fluid inclusions with multiple daughter minerals that include halite, sylvite, hematite, and up to four additional, unidentified opaque and nonopaque minerals (Table 2). The remaining inclusions are vapor-rich with <10 percent visible liquid. Limited microthermometric data indicate trapping temperatures between 315° and 675°C and salinities between 35 and 84 wt percent NaCl equiv.

In zones where A-veinlets rather than banded quartz veinlets predominate, copper strongly correlates with gold (Fig. 4A), hypogene copper grades are mostly between 0.1 to 0.4

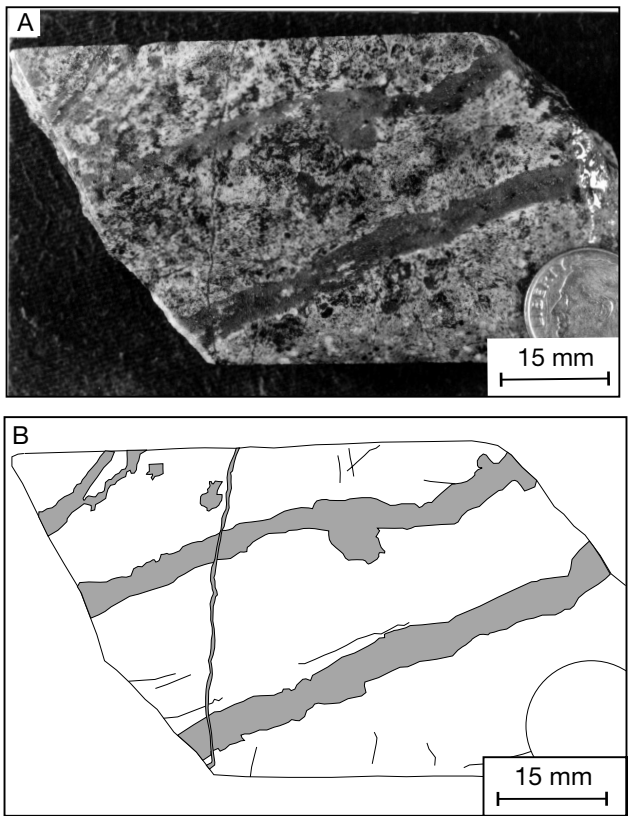

FIG. 3. Example of A-veinlets in drill core sample from the Cerro Casale porphyry gold-copper deposit at Aldebarán. A. Photograph. B. Explanation. Note irregular vein walls that do not match. Host rock is a fine-grained feldspar porphyry dike. The dark patches are partially chloritized hydrothermal biotite.

TABLE 1. Summary of Vein Types

		Vein center or vein filling							Wall-rock alteration halo			Age relative to other veins	
		Major		Minor									
Vein type	Location	Gangue	Opaque	Gangue	Opaque	Thickness	Length	Sructure	Major	Minor	Thickness	Postdate	Predate
A-veinlets													
A-1	Pan, Cas, Cav	bio-qtz	mt-cp	None	py, sl	<0.2 mm	cm's	Irregular walls	bio, ksp, ksp-olig, ksp-qtz	None	<0.1 mm	A-2,4	A-2,3 4,5, banded qtz vnlts, D-vns
A-2	Pan, Cas	qtz	mt-cp	ksp, chl, bio, gyp, ser[3]	spec[3]	<1 cm	10s cm	Irregular walls	ksp-chl[3]	ser[3]	<1 mm	A-1	A-1,3,4, banded qtz vnlts, D-vns
A-3	Cas	qtz-ksp	spec	None	cp	<1 cm	10s cm	Irregular walls	ksp	None	<1 mm	A-1,2,3	A-4, banded qtz vnlts, D-vns
A-4	Pan, Cas	qtz	cp	None	py	<1 cm	10s cm	Straight walls	None	None		A-1,2,3	A-1, banded qtz vnlts, D-vns
A-5	Cav	qtz	py-mt	None	cp	<2 cm	m's	Straight walls	None	None		A-1, banded qtz vnlts	banded quartz veinlets, D-vns, qtz-alun ledges
Banded quartz veinlets													
Outside dark bands:	Ver, Pan, Cas, Cav	qtz-ksp-cal-chl	py-mt	ill, ep, gyp, gar, tour, spn	cp, sl, spec, gl, mo, cas	<2 cm	10s cm to m's	Slightly wavy parallel walls	None	None		A-vnlts	A-5[4], D-veins, qtz-alun ledges[5]
Inside dark bands:	Ver, Pan, Cas, Cav	qtz	mt	None	cp, bn, sl	0.001-0.1mm	10s cm to m's	Symmetric pairs, streaks	None	None			
D-veins	Pan, Cas, Cav	qtz	py	ser	cp, mo, spec, bn, ten, en, gl, cas	<1 mm to cm's	1-10 m	Straight walls	qtz-ser-py	tour, rt	mm's to cm's	A-vnlts, banded qtz vnlts	
Polymetallic:	Cas[1]	qtz-bar	py	ser	cp, sl, ten, tet, gl	cm's to 10s cm	10s to 100s m's	Straight walls	qtz-ser-py	tour, rt	cm's to 10s cm	A-vnlts	
Quartz-alunite ledges													
QA-1	Ver, Pan, Cas[1], Cav[2]	qtz-alun	py	rt, dick, dia, bar	None	0.5-5 m	10s m	Replacement	qtz-kao-py, qtz-ser-py"	tour, rt	m's	A-vnlts, banded qtz vnlts[5]	
QA-2	Cas[1], Cav[2]	qtz-alun-bar-chal	py-en	rt, dia	cov	0.5-5 m	10s to 100s m's	Replacement	qtz-kao-py, qtz-ser-py	pyro, rt m's			

Abbreviations: Cas = Cerro Casale, Cav = Cavancha, Pan = Pancho, Ver = Verde, irreg = irregular, vns = veins, vnlts = veinlets

Mineral abbreviations: alun = alunite, bar = barite, bio = biotite, bn = bornite, cal = calcite, cas = cassiterite, chal = chalcedony, chl = chlorite, cp = chalcopyrite, cov = covellite, dia = diaspore, dick = dickite, en = enargite, ep = epidote, gar = garnet (andradite), gl = galena, gyp = gypsum, ill = illite, kao = kaolinite, ksp = K feldspar, mo = molybdenite, mt = magnetite, olig = oligoclase, py = pyrite, qtz = quartz, pyro = pyrophylllite, rt = rutile, ser = sericite, sl = sylvite, spec = specular hematite, spn = sphene, ten = tennantite, tet = tetrahedrite, tour = tourmaline

[1] Aldebarán district as well as Cerro Casale

[2] La Pepa district as well as Cavancha

[3] Seen only at Cerro Casale

[4] Relation seen only at Cavancha

[5] Relationship seen only at Verde

TABLE 2. Characteristics of Fluid Inclusions[1]

Vein type	Temperature (°C)	Salinity (wt %)[2]	Description of inclusions
A-veinlets[3]	315–675[4]	35–84	Liquid-rich inclusions with multiple daughter minerals coexisting with vapor-rich inclusions; smooth equant to negative crystal shapes
Banded quartz veinlets[5]	220–350[4]	3.4–33	>99% vapor-rich inclusions coexisting with liquid-rich inclusions with or without daughter minerals; smooth equant shapes
D-veins	<400[6]	>26 and <26[7]	Liquid-rich inclusions with or without daughter minerals coexisting with vapor-rich inclusions; irregular shapes
Quartz-alunite ledges	?	<26[7]	Liquid-rich inclusions without daughter minerals coexisting with vapor-rich inclusions

[1] Additional information, including methodology, is found in Appendix
[2] Wt % NaCl equivalent
[3] Microthermometric data were collected from three samples
[4] Trapping temperatures of fluid inclusions
[5] Microthermometric data were collected from five samples
[6] The brittle nature of the veins, irregular shapes of fluid inclusions, and microthermometric data collected from one sample suggest temperatures less than 400°C, which is the estimated temperature of the brittle-ductile transition
[7] 26 refers to the wt percent of NaCl above which a halite daughter mineral will be present at room temperature

wt percent, and gold grades are <1 ppm. Multielement analyses of six samples in which A-veinlets predominate show low silver concentrations with silver/gold ratios ranging from 0.3 to 1.4 (Table 3).

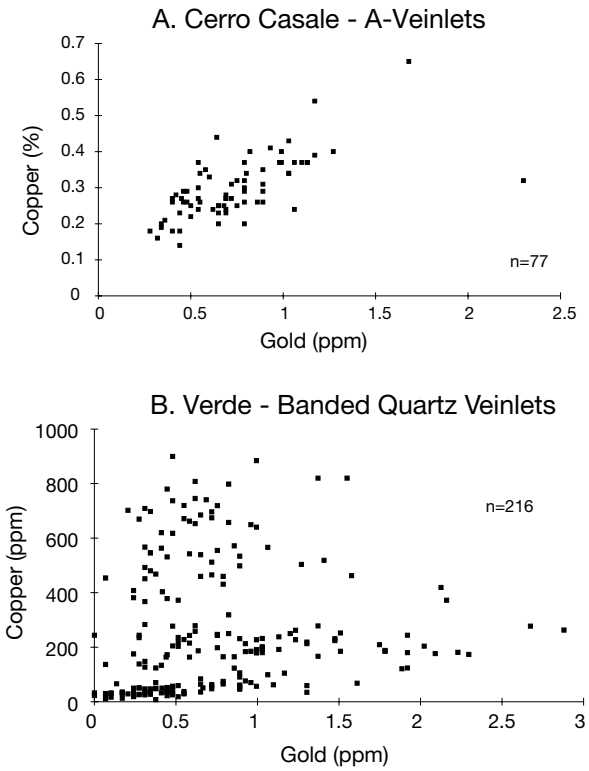

FIG. 4. Plots of copper vs. gold grades of unoxidized, unenriched (no supergene chalcocite) intervals. Individual points in each plot represent bulk assays of drill core intervals ranging from 0.2 to 2 m. A. Assays from three logged core holes from Cerro Casale where A-veinlets are the predominant vein type. B. Assays from 10 logged core holes from Verde where banded quartz veinlets are the predominant vein type.

Banded quartz veinlets

Banded quartz veinlets are characterized by bands of dark gray to black quartz that commonly occur as symmetric pairs near the margins of hairline to millimeter-wide quartz veins that lack alteration envelopes (Fig. 5, Table 1). Quartz is mostly granular but grains elongated perpendicular to the vein walls also are found. Vein centers are locally vuggy and vein walls are parallel and slightly wavy. We conclude that banded quartz veinlets form by open-space filling. Banded quartz veinlets cut and offset A-veinlets. The reverse relationship has been seen in a few cases at La Pepa. Intrusions locally truncate banded quartz veinlets and/or incorporate banded quartz veinlets as fragments.

The darkness of the bands reflects the presence of abundant vapor-rich fluid inclusions and micron-size magnetite. Dark bands also contain rare micron-size chalcopyrite, bornite, and sphalerite encapsulated in quartz. Pyrite has not been noted as part of the assemblage. The dark bands are locally botryoidal and are commonly continuous through quartz grains suggesting recrystallization from a silica gel (cf. Boydell, 1924; Ramdohr, 1980; Sander and Black, 1988; Saunders, 1994). Pyrite and gangue minerals other than quartz commonly fill the vuggy vein centers, a relationship also noted by Vila et al. (1991) in banded veinlets at Marte, and fill fractures that cut the banded veinlets. Where in grain contact with magnetite, pyrite has partially replaced magnetite. These relationships indicate that pyrite postdates both magnetite and the copper-iron sulfides, and it may be later than the banded quartz veinlets. Total content of magnetite, sulfide, and nonquartz gangue is generally <5 vol percent.

Fluid inclusions in banded quartz veinlets are described by Muntean and Einaudi (2000). To summarize, >99 percent of the fluid inclusions are vapor-rich with no visible liquid, and <1 percent are liquid-rich with or without a halite daughter mineral (Table 2). In addition to halite, rare inclusions contain up to three unidentified opaque and nonopaque daughter minerals. The proportion of vapor-rich inclusions to

TABLE 3. Multielement Analyses of the Four Main Vein Types

Sample	Location	Oxidized	Au (ppb)	Ag (ppm)	Cu (ppm)	Pb (ppm)	Zn (ppm)	Mo (ppm)	As (ppm)	Sb (ppm)	Hg (ppb)	Bi (ppm)	Sn (ppm)	Te (ppm)	Se (ppm)	Cd (ppm)	Ba (ppm)	Mn (ppm)
A-veinlets[1]																		
LYR-2 48-50.5m	Pancho	no	1,640	0.5	2,000	13	798	4.3	7.2	0.1	10	0.1	8	0.85	0.4	2.2	513	1,080
LYR-3 44-46m	Pancho	no	826	0.3	1220	14	484	13.6	3.6	0.1	10	0.1	17	0.74	0.5	3.8	549	1,940
ALC-1 272m	Casale	no	452	0.8	4,310	40	47.5	4.5	8.0	2.5	90	0.2	9	0.28	0.9	0.8	4,950	40
DD-4 72-74m[3]	Casale	no	661	0.9	2,970	13	156	25.7	1.3	0.2	6	0.7	12	1.12	1.0	<0.2	456	310
CAV-2 271.5m	Cavancha	no	114	0.1	269	2	168	5.3	84.4	0.4	12	0.4	<5	0.42	<0.1	<0.2	560	1,440
CAV Adit 182-184m	Cavancha	no	542	0.7	913	18	39.8	18.3	23.2	0.6	10	1.4	<5	1.21	1.3	<0.2	432	<100
Banded quartz veinlets[2]																		
DD-10 160-165m	Verde	no	564	0.7	641	10	400	40.6	84.0	0.2	19	0.3	10	1.29	0.1	<0.2	565	1,860
DD-26 106-112m	Verde	no	714	0.2	357	16	524	42.3	15.2	0.2	12	0.2	15	1.30	0.1	<0.2	573	5,580
DD-26 34-40m	Verde	yes	1,190	<0.2	136	11	503	25.4	19.2	0.1	7	0.2	<5	1.29	0.3	<0.2	577	1,940
VDM10 35-50m	Verde	yes	1,080	<0.2	646	5	203	10.7	9.3	0.4	7	0.3	<5	0.46	<0.1	<0.2	1,620	960
VDM19 30.6-46m	Verde	yes	1,250	<0.2	672	97	742	8.0	6.0	0.4	31	0.2	16	0.24	<0.1	1.3	593	2,600
D-veins																		
AVZ95-11	Aldebarán, polymetallic	no	1,040	136	1,350	737	1510	0.2	4,000	3,250	17,400	221	23	0.51	<0.1	13.2	715	267
ALC-1 259m	Casale, polymetallic	no	374	340	41,800	22,400	2,280	123	364	260	2,280	0.3	<5	0.57	94.9	12.5	13%	39
ALC-1 19.9m	Casale, polymetallic	yes	234	80.3	706	648	32.6	69.3	500	405	12,000	0.5	6	0.39	0.5	<0.2	23,900	29
ACS013[3]	Aldebarán, polymetallic	yes	168	309	448	74,800	211	16.6	770	740	34,150	0.6	<5	0.88	0.3	10.4	22,800	18
ACS021	Aldebarán, polymetallic	yes	100	18.3	22.3	440	27.6	618	37.8	20.0	856	0.5	17	1.21	0.5	<0.2	10,500	11
ACSDM1-6	Casale, tourmaline breccia	yes	113	2.2	51.5	101	16.1	67.5	16.1	4.2	34	0.5	27	0.55	0.6	<0.2	2,020	54
CAV-2 252.4	Cavancha	no	12,000	4.1	2,170	34	325	61.3	88.9	2.1	59	4.4	12	18.8	0.4	<0.2	469	10
Quartz-alunite ledges																		
RR001	Refugio	yes	8	<0.2	1.4	<1	0.9	3.6	1.1	0.2	6	0.1	<5	0.31	0.2	<0.2	1,050	20
RP035	Refugio	yes	19	<0.2	7.2	18	9.4	5.3	60.4	0.5	<5	0.8	8	1.68	1.9	<0.2	1,600	5
RP030	Pancho	yes	96	0.3	17.4	2	7.5	0.9	27.1	0.6	8	0.2	11	0.60	1.0	<0.2	535	11
RP029	Pancho	yes	58	0.9	97.6	38	2.6	4.5	196	13.1	9	0.3	<5	1.09	0.4	<0.2	792	8
RV093[c]	Verde	yes	694	9.5	31.6	34	9.8	41.2	397	38.1	74	6.4	<5	1.06	0.4	<0.2	29,000	16
VDM12 17.7-18m[3]	Verde	yes	724	2.0	36.8	19	9.9	53.3	343	5.9	16	0.5	16	1.24	1.2	<0.2	1,610	49
AVZ005	Aldebarán	yes	17	0.7	97.3	55	8.9	0.4	239	3.4	28	0.2	11	0.24	0.7	<0.2	1,570	8
AVZ95-6-1[3]	Aldebarán	yes	17	0.5	111	17	15.7	4.8	397	7.8	114	0.8	<5	0.49	0.2	<0.2	1,240	137
AVZ95-9	Aldebarán	yes	131	2.5	25.6	15	5.7	26.7	27.1	2.6	36	0.2	<5	0.18	1.4	<0.2	6,910	430
ACS95-3	Aldebarán	yes	4	1.6	15.6	300	28.2	28.6	33.3	5.1	200	0.1	<5	0.38	0.4	<0.2	2,620	280
ACT010	Aldebarán	yes	3	0.3	<0.5	48	1.5	4.0	3.5	0.8	203	0.1	7	2.16	1.1	<0.2	512	8
ACT95-1	Aldebarán	yes	737	81.1	95.1	112	19.4	8.7	3,740	230	4,710	18.7	<5	3.73	<0.1	<0.2	71,000	114
AVZ95-17	Aldebarán	no	118	10.7	609	30	106	16.0	4,300	126	699	4.8	9	0.48	<0.1	<0.2	5,890	305
LP012	La Pepa	no	9,360	66.7	44,300	10	69.2	0.2	24,600	220	1,100	3.6	75	1.98	<0.1	1.5	1,960	15
Gema Vein	La Pepa	yes	1,780	10.3	22.6	23	11.4	0.9	78.4	0.3	107	5.8	30	3.79	1.4	<0.2	2,300	<100

Samples were analyzed by XRAL Laboratories, Toronto, Canada. Analytical methods and sample descriptions and locations are described in Muntean, 1998

[1]Samples where A-veinlets are the dominant vein type

[2]Samples where banded quartz veinlets are the dominant vein type

[3]Average of two duplicate analyses

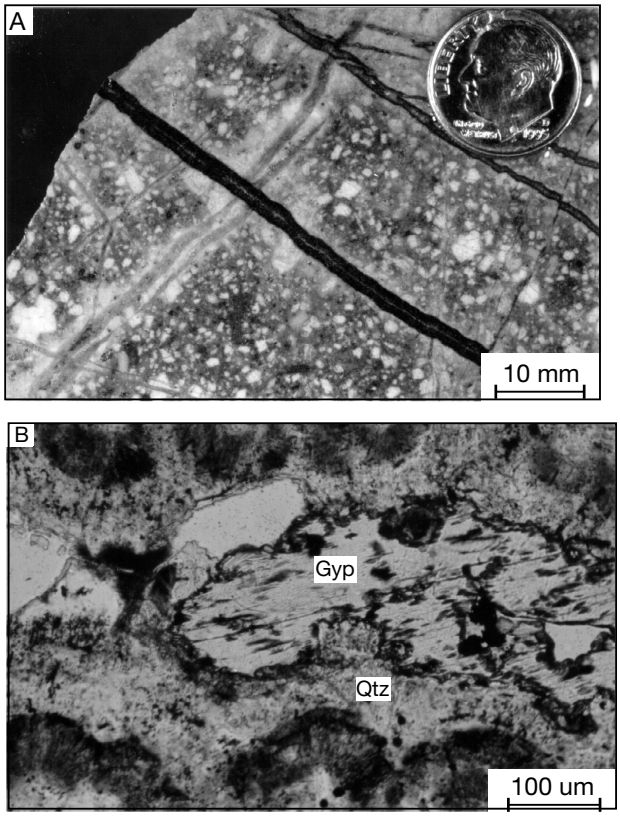

FIG. 5. Banded quartz veinlets from Refugio. A. Banded quartz veinlets (dark) cutting and offsetting A-veinlets (light), from the Pancho deposit. Apparent alteration envelopes are the result of supergene alteration. B. Photomicrograph of banded veinlet showing botryoidal banding, from Verde orebody, uncrossed polars. Dark bands contain abundant micron-sized magnetite and vapor-rich fluid inclusions. The mineral with the cleavages in the vuggy vein center is gypsum (Gyp) with pyrite inclusions. Qtz = quartz.

liquid-rich inclusions is the same inside or outside of the dark bands, but the dark bands contain more abundant fluid inclusions. Coexisting vapor-rich and liquid-rich inclusions occur in growth zones represented by the dark bands, on either side of the dark bands, and in individual secondary planes that cut growth features. Trapping temperatures of liquid-rich inclusions coexisting with vapor-rich inclusions range from 220° to 350°C, whereas salinities range from 3.4 to 34 wt percent NaCl equiv. Fluid inclusions in the dark bands are primary in origin with respect to quartz but not with respect to silica gel. Because gold, magnetite, and rare copper-iron sulfides in the dark bands likely were deposited with the silica gel, the fluid inclusions do not record the conditions of gold deposition. On the other hand, the paragenetically later gold associated with pyrite and gangue minerals may have been deposited from fluids similar to those that that formed the recrystallized quartz.

At the four deposits studied, zones where banded quartz veinlets predominate typically contain 0.5 to 2 ppm gold and less than 0.1 wt percent hypogene copper, indicating higher gold/copper ratios than in zones where A-veinlets predominate. On the basis of assays of ten core holes from the Verde orebody, where banded quartz veinlets are the dominant vein type, there is no correlation between copper and gold contents (Fig. 4B). The majority of assay intervals of drill core at Verde contain <1.7 ppm silver, and multielement analyses of five samples with banded veins from Verde show silver/gold ratios ranging from <0.16 to 1.2 (Table 3).

D-veins

D-veins are pyrite veins with minor amounts of quartz. They tend to be thicker (up to 10 cm) and more continuous (up to 10 m) than A-veinlets, have fairly straight walls, and are locally vuggy. These veins formed by open-space filling. Quartz-sericite-pyrite halos with local tourmaline (Table 1) are characteristic, and advanced argillic assemblages are absent. In any given deposit, D-veins cut and offset A-veinlets, banded quartz veinlets, and all intrusions. The opposite relationship has not been observed.

Quartz in D-veins is clear and euhedral with very fine growth zones marked by submicron fluid inclusions. Where visible, vapor-rich inclusions coexist with liquid-rich inclusions with or without halite and other daughter minerals (Table 2). The brittle nature of the veins, irregular shapes of fluid inclusions, and very limited microthermometric data suggest temperatures less than 400ºC. Details concerning the mineralogy and relations to copper and gold are presented below in the descriptions of individual deposits.

Quartz-alunite ledges

Quartz-alunite ledges are steeply dipping replacement veins typical of high-sulfidation epithermal deposits worldwide. In the Maricunga belt, quartz-alunite ledges have widths of centimeters to meters and strike lengths mostly on the order of tens of meters. The ledge material consists of quartz + alunite + pyrite + rutile and contains local kaolinite, dickite, diaspore, or pyrophyllite as well as local core zones of residual vuggy quartz. Quartz has a fine-grained granular or jigsaw-like texture and is mostly of replacement origin.

Euhedral quartz crystals, barite and/or enargite commonly line open spaces in vuggy quartz zones or occur along fractures toward the centers of ledges. The euhedral quartz crystals locally have growth zones marked by tiny (<2 μm) primary vapor-rich inclusions and coexisting liquid-rich inclusions without halite daughter minerals (Table 2). Limited infrared microscopy failed to detect any fluid inclusions in enargite.

The strongest evidence that alunite is hypogene is its coarse grain size, bladed crystal habit (cf. Hedenquist et al., 2000), and association with dickite or diaspore; its close association with pyrite is consistent with a hypogene origin. Stable isotope studies of similar alunite occurrences elsewhere have shown that such alunite forms from magmatic vapor condensed into meteoric water at temperatures typically greater than 200°C; such alunite is termed magmatic-hydrothermal alunite (Rye et al., 1992; Arribas, 1995).

Where unequivocal crosscutting relationships are found, quartz-alunite ledges postdate A-veinlets and banded quartz veinlets. The opposite relationship has not been observed. Moreover, no quartz-alunite ledges are cut by intrusions.

Most of the quartz-alunite ledges at Refugio and Aldebarán have subeconomic gold grades; however, mineable bonanza grades occur at La Pepa. Samples of quartz-alunite ledges contain higher silver/gold ratios (>2.8) and higher arsenic, antimony, mercury, bismuth, tin, and tellurium concentrations

than samples containing A-veinlets or banded quartz veinlets (Table 3).

Refugio District

Introduction

The Refugio district contains two gold deposits, Verde and Pancho, hosted by early Miocene andesitic to dacitic volcanic and intrusive rocks (Vila and Sillitoe, 1991; Flores, 1993; Muntean and Einaudi, 2000). Zones of quartz veinlets are closely linked in time and space to quartz diorite porphyry stocks and related bodies of intrusive breccia (Fig. 6). Intrusive breccias (cf. Wright and Bowes, 1963) have well-defined fragments of immediate wall rock and poorly defined autoliths of quartz diorite porphyry in an igneous matrix with textures that locally suggest fluidization (Muntean and Einaudi, 2000). They are common in all of the porphyry gold deposits in the Maricunga belt.

The mineable reserve at Verde just before commencement of mining in late 1995 was 101 million tonnes (Mt) of 1.02 g/t gold at a cut-off grade of 0.5 g/t (Brown and Rayment, 1991). The average copper grade is 0.03 percent (Flores, 1993), with little difference between oxidized and unoxidized ores. Pancho has a drill-inferred resource of 68 Mt of 0.96 g/t Au (Brown and Rayment, 1991). Drill hole assays at Pancho indicate hypogene copper grades between 0.05 and 0.2 percent. The Verde and Pancho deposits were mapped in detail, as outlined in Muntean and Einaudi (2000).

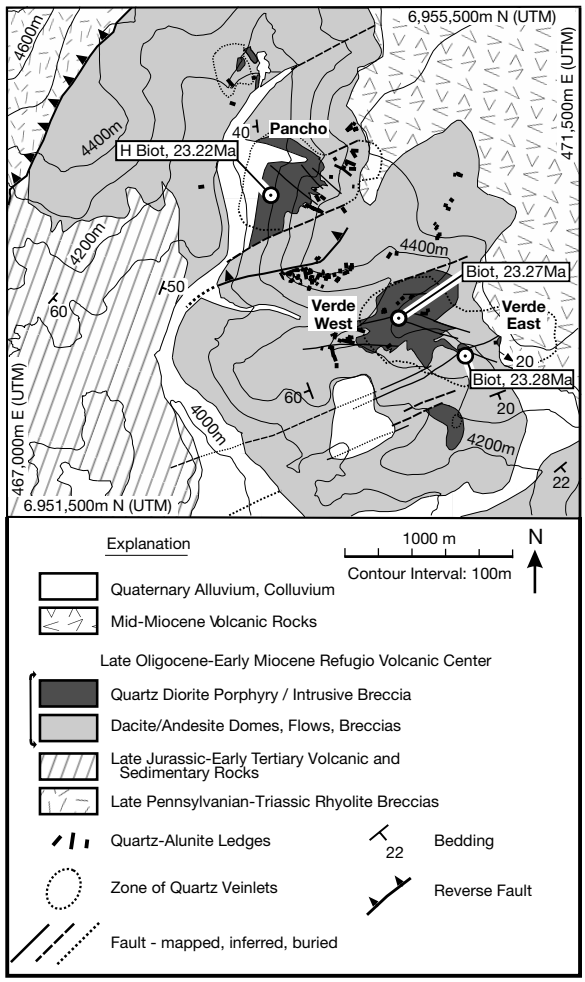

FIG. 6. District geology map of Refugio, modified from Muntean and Einaudi (2000). Shows $^{40}Ar/^{39}Ar$ dates and sample locations. Biot = igneous biotite, H Biot = hydrothermal biotite.

Verde deposit

Orebodies at Verde (Verde West and Verde East) are coincident with radial and concentric patterns of banded quartz veinlets that are centered on late stocks of quartz diorite porphyry. The stocks truncate banded quartz veinlets at their contacts. The late stocks are emplaced into bodies of intrusive breccia and/or earlier intrusions of dacite porphyry that are pervasively replaced by a chlorite-magnetite-albite assemblage. Ore generally contains 1 to 4 vol percent magnetite and mostly <1 vol percent pyrite >> chalcopyrite. The ore zone is surrounded by pyrite-albite-clay assemblages with 2 to 4 vol percent pyrite. This distal assemblage may have formed contemporaneously with the inner chlorite-magnetite-albite assemblage and encroached upon the latter with time, as demonstrated by local replacement of magnetite by pyrite.

Banded quartz veinlets make up >99 percent of the veins at Verde and are the feature most closely associated with gold. A-veinlets have not been documented at Verde within the 500 m vertical range of exposure. Quartz-alunite ledges postdate the banded quartz veinlets, and D-veins are absent.

Pancho deposit

Pancho, exposed along a 30- to 40-degree slope throughout a vertical interval of about 400 m (Fig. 7), contains all four vein types. Intrusive rocks compose the lower half of the hillside and consist of an early quartz diorite porphyry stock cut by dikes of intrusive breccia and aplite. A-veinlets are restricted to intrusive rocks, and most occur in rocks altered to potassic assemblages. Central magnetite-K feldspar-oligoclase assemblages (central potassic zone) and outer hydrothermal biotite (outer potassic zone) are restricted to intrusive rocks. These zones are variably overprinted by chlorite. Magnetite content is mostly 2 to 5 vol percent, but it reaches 10 percent locally in the central potassic zone where it is accompanied locally by specular hematite. Sulfide content and pyrite/chalcopyrite ratios are mostly <1 vol percent and <1, respectively, in the central potassic zone and <2 vol percent and slightly >1, respectively, in the outer potassic zone.

Banded quartz veinlets are present throughout Pancho but are most abundant in the upper levels of the intrusion. Banded quartz veinlets in all cases cut and offset A-veinlets. Their abundance decreases in the overlying volcanic rocks where they mostly occur as sheeted sets.

Intrusive breccia and aplite dikes truncate A-veinlets and banded quartz veinlets in quartz diorite porphyry, contain veined fragments of quartz diorite porphyry, and are cut by A-veinlets and banded quartz veinlets. Parts of the quartz diorite porphyry stock lack potassic assemblages or quartz veinlets. Thus, the bulk of the quartz veinlets and gold-copper deposits appear to have formed during intrusion of the dikes.

Volcanic rocks are replaced by pervasive pyrite-albite-clay, which also overprints the potassic assemblages at the highest

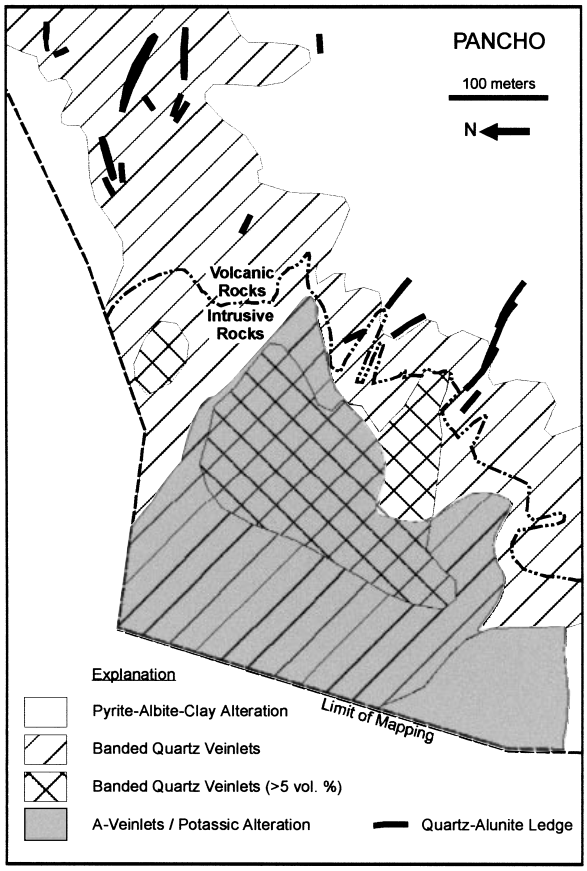

FIG. 7. Map of hydrothermal alteration and vein types at the Pancho deposit at Refugio, modified from Muntean and Einaudi (2000).

levels of the intrusion. D-veins occur locally in the potassic zones and in the lower parts of the pyrite-albite-clay zone. Where crosscutting relationships are observed, D-veins cut and offset both A-veinlets and banded quartz veinlets. D-veins are not truncated by intrusions and must have formed after all intrusions were emplaced. Quartz-alunite ledges are restricted to volcanic rocks. No unequivocal crosscutting relationships were documented between quartz-alunite ledges and banded quartz veinlets or D-veins at Pancho.

Aldebarán District

Introduction

In the Aldebarán district (Vila and Sillitoe, 1991), hydrothermally altered rocks are exposed for 5 km in a vertical range of about 1,100 m (Fig. 8). A porphyry gold-copper deposit, Cerro Casale, is exposed on the eastern side of the district at elevations between 4,100 and 4,400 m. The deposit is coincident with a zone of quartz veinlets that are hosted by a composite intrusion. Drilling indicates that the deposit extends to depths >1 km and contains a measured and indicated resource of 1,114 Mt of 0.71 g/t gold and 0.26 percent Cu (R. Pease, pers. commun., 2000). Numerous subeconomic quartz-alunite ledges and polymetallic veins crop out within the alteration zone west of Cerro Casale in sectors referred to as the Vein zone and Cerro Catedrál at elevations up to 5,093 m (Vila and Sillitoe, 1991) (Fig. 8). To document the vein relationships at Cerro Casale, 2 km of road cuts (much of the western half of the deposit) were mapped, three core holes were logged, and 250 sawed samples and 58 polished thin sections were examined.

Early alteration and mineralization events, Cerro Casale

The bulk of the composite intrusion at Cerro Casale is a medium-grained quartz diorite porphyry (Fig. 9A). The early quartz diorite porphyry is cut by numerous irregular dikes of fine-grained feldspar porphyry, aplite, and intrusive breccia. The dikes, referred to here as feldspar porphyry dikes, are strongly altered to potassic assemblages, whereas parts of the early quartz diorite porphyry stock lack potassic assemblages or quartz veinlets. The dikes truncate A-veinlets in quartz diorite porphyry, contain veined fragments of quartz diorite porphyry, and are cut by abundant A-veinlets. Thus, the feldspar porphyry dikes clearly were emplaced during the mineralization episode. The final igneous phase is a weakly mineralized (<0.5 ppm Au), medium-grained biotite porphyry that occurs as dikes truncating quartz veinlets in earlier intrusive phases.

Potassic assemblages (Fig. 9B) include peripheral biotite and central, deep K feldspar + quartz. In the zone of hydrothermal biotite, hornblende phenocrysts and portions of biotite phenocrysts are replaced by aggregates of fine-grained, shreddy-textured, hydrothermal biotite. Abundant biotite occurs also in the porphyry groundmass and magnetite abundance is mostly between 1 and 5 vol percent. Original rock texture is preserved. In central and deeper zones, porphyry groundmass is replaced by aggregates of quartz and perthitic alkali feldspar, and plagioclase phenocrysts are partially replaced by K feldspar. With increasing development of the K feldspar-quartz assemblage, brownish biotite is replaced by green biotite with or without chlorite and sericite, particularly near A-veinlets. In intensely altered rock, plagioclase phenocrysts, biotite, and groundmass are completely replaced by interlocking grains of ragged perthitic K feldspar and quartz up to several hundred microns in size. Rock texture is obliterated, magnetite is commonly altered to hematite along grain boundaries, and specular hematite is present locally. Total magnetite + hematite content is mostly between 4 and 7 vol percent and locally up to 10 vol percent.

A-veinlets are restricted to potassic alteration zones, where their abundance ranges from 1 to 10 vol percent and locally up to 20 vol percent (Fig. 9B). A-veinlets are most abundant in feldspar porphyry dikes or along the margins of such dikes and decrease to <1 vol percent in the late biotite porphyry. Chalcopyrite, mostly <1 vol percent, is the only sulfide in A-veinlets and is also disseminated in potassic zones, where it is closely associated with magnetite and specular hematite. Late fractures filled with gypsum are very common in potassic zones at the top of the unoxidized zone. Deeper gypsum is locally present in A-veinlets where it commonly contains iron-oxide and chalcopyrite inclusions, suggesting that anhydrite was present prior to weathering.

Banded quartz veinlets have been identified only at the surface at elevations above 4,300 m, mostly peripheral to the Cerro Casale orebody, where they constitute <2 vol percent of the rock (Table 1, Fig. 9B). They cut quartz diorite porphyry, feldspar porphyry dikes, and A-veinlets.

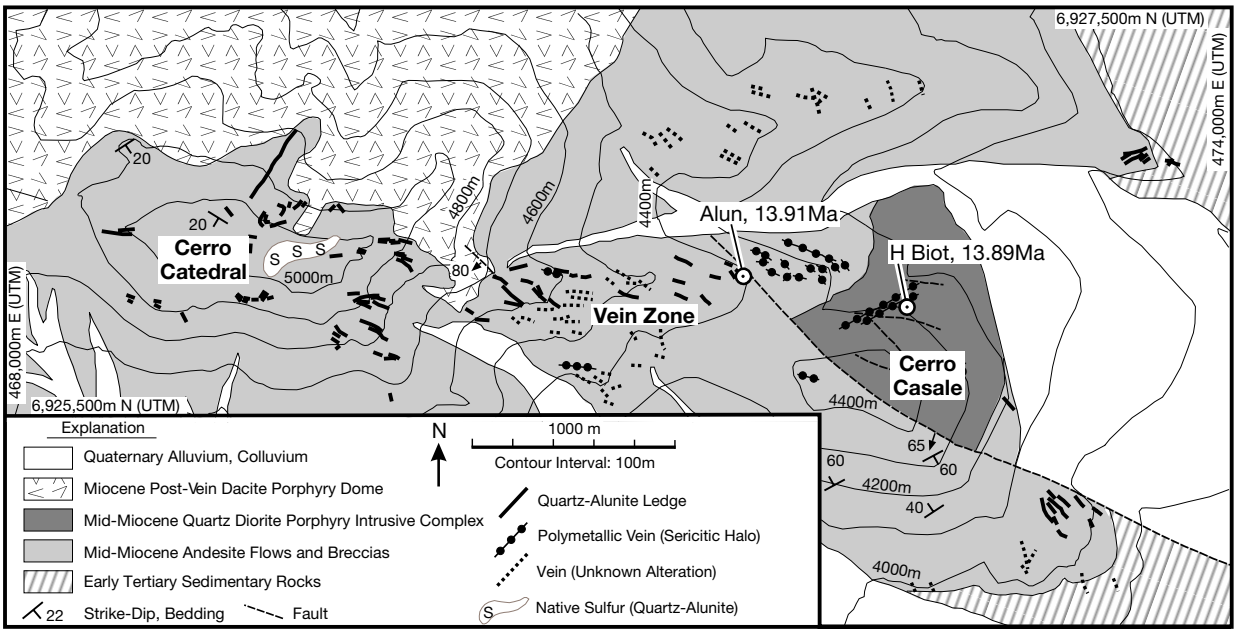

FIG. 8. District geology map of Aldebarán. Based mostly on unpublished mapping by Anglo-American geologists and mapping completed during this study. Shows $^{40}Ar/^{39}Ar$ dates and sample locations. "Vein (Unknown Alteration)" refers to veins not examined during this study, and distinction between quartz-alunite ledge and polymetallic veins was not possible given available information. Alun = alunite, H Biot = hydrothermal biotite.

Late mineralization at Cerro Casale and Vein zone

Tourmaline-bearing hydrothermal breccia, pyrite-albite-clay assemblages, D-veins, and polymetallic veins postdate all intrusions at Cerro Casale. The tourmaline-bearing hydrothermal breccia (Fig. 9) contains 75 to 90 percent angular fragments of highly altered porphyry in a clay-rich, rock flour matrix. Fragments contain A-veinlets and/or banded quartz veinlets truncated at the fragment margins. Locally the matrix is vuggy, incompletely filled by hydrothermal quartz with about 10 percent tourmaline and with local, minor gypsum, specular hematite, chalcopyrite, and bornite. Quartz-specular hematite veinlets, originating in the breccia matrix, extend tens of meters into the bordering country rocks. A clay-rich zone of bleached rock appears to be centered on the tourmaline breccia (Fig. 9B). This zone consists mostly of quartz, illite and albite with 2 to 4 vol percent specular hematite and/or pyrite and tourmaline. Illite, as referred to in this study, has a d(001) of 10 Å and a crystal size $<5\ \mu$m.

D-veins, containing >50 vol percent pyrite, lesser quartz, and up to 5 vol percent chalcopyrite, are widespread at Cerro Casale and locally fill reopened A-veinlets. In a few occurrences, specular hematite is present instead of pyrite. D-veins cut all intrusions, A-veinlets, banded quartz veinlets, and the tourmaline breccia. Reverse age relationships have not been observed.

Polymetallic veins were mapped on the northern and western sides of Cerro Casale (Figs. 8, 9B). They are up to 20 cm wide and have straight walls. The veins contain euhedral quartz, about 10 to 25 vol percent barite, minor sericite, and indigenous limonite that suggest about 25 to 50 vol percent sulfides. They have centimeter-scale quartz-sericite-pyrite halos that are very similar to those associated with D-veins. Core samples with rare relict sulfides contain intergrown pyrite, chalcopyrite, sphalerite, and tetrahedrite/tennantite. The veins commonly contain >100 ppm silver and several percent lead; multielement analyses of five samples also show elevated copper, zinc, molybdenum, arsenic, antimony, mercury, and cadmium concentrations (Table 3). Polymetallic veins cut quartz diorite porphyry, dike rocks, and A-veinlets. Their temporal relationship with D-veins has not been established.

Vila and Sillitoe (1991) defined a Vein zone with a strong Ag-Pb-Zn-Sb soil anomaly extending 1.5 km west of Cerro Casale (Fig. 8). Veins contain several percent lead and zinc, up to 200 ppm Ag, but <1 g/t Au. The veins have sulfide assemblages and alteration halos similar to the polymetallic veins at Cerro Casale.

Quartz-alunite ledges in Vein zone and Cerro Catedrál

Quartz-alunite ledges, hosted by volcanic rocks and generally containing <1 ppm Au (Vila and Sillitoe, 1991; Table 3), are particularly abundant in the Vein zone and at Cerro Catedrál, located 4 km west of Cerro Casale (Fig. 8). The ledges are spatially separated from intrusions, potassic alteration zones, A-veinlets, banded quartz veinlets, and D-veins; therefore, relative age relationships are indeterminate. Although the dominant trend is west to northwest, ledges display weak radial patterns around Cerro Casale and Cerro Catedrál.

Widespread bleached and iron-stained rocks in the Vein zone and Cerro Catedrál contain quartz, pyrite, and unidentified clay in green, unweathered samples. Advanced argillic assemblages at Cerro Catedrál are limited to narrow quartz-alunite ledges and their immediate wall rocks. Ledges below elevations of about 4,600 m consist of quartz, alunite, pyrite,

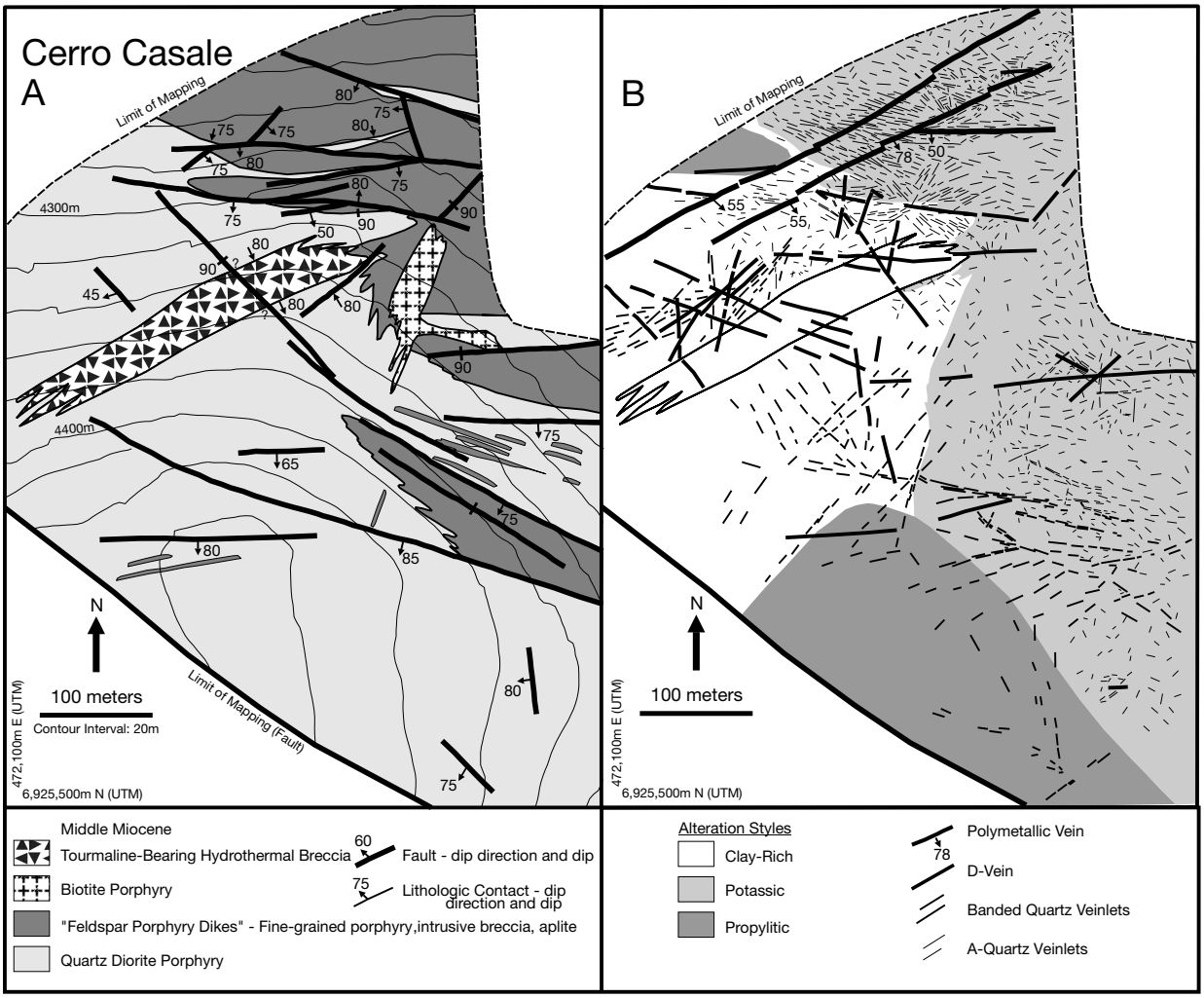

FIG. 9. Geologic map (A) and map of alteration and vein types (B) of the western part of the Cerro Casale orebody, Aldebarán, on the basis of mapping completed during this study in 1995. A-veinlets, banded quartz veinlets, and D-veins are not drawn to scale.

and rutile. Pyrite content, estimated from relict unoxidized zones and leached cavities, ranges from 2 to 10 vol percent. Ledges are surrounded by meter-scale alteration halos that are zoned from inner alunite-quartz with local pyrophyllite to outer quartz-kaolinite or quartz-sericite with disseminated tourmaline. Ledges above about 4,600 m elevation along the flanks of Cerro Catedrál consist of a central core of vuggy residual quartz with pyrite, rutile, and local alunite and diaspore, locally cut by enargite-quartz veinlets. Vuggy quartz contains abundant coarse-grained, bladed barite above 4,800 m elevation and native sulfur with elevated mercury above 5,000 m as noted by Vila and Sillitoe (1991).

La Pepa

Introduction

Both Refugio and Aldebarán have abundant quartz-alunite ledges, most containing <1 ppm Au. By contrast, quartz-alunite ledges at La Pepa average about 20 ppm Au, locally contain up to 1,000 ppm Au, and have produced approximately 250,000 oz of gold (A. Valverde, pers. commun., 1993). An erosional window through a late Miocene ignimbrite exposes highly altered late Oligocene to early Miocene volcaniclastic rocks and lesser porphyry dikes and stocks (Fig. 10). The quartz-alunite ledges, some of which were being mined by Compañia Minera La Pepa at the time of this study, are located above and peripheral to a small porphyry gold deposit known as Cavancha. Key surface outcrops and underground exposures of quartz-alunite ledges were visited with Minera La Pepa geologists in 1993 and 1995, and an adit through the Cavancha deposit was mapped. Three core holes were logged, and 80 sawed samples and 32 polished thin sections were examined.

Cavancha porphyry gold deposit

Cavancha is hosted by multiple intrusions of quartz diorite porphyry and intrusive breccia similar to the feldspar porphyry dikes at Cerro Casale. The area of intrusive rock and quartz veinlets is approximately 400 m in diameter and occurs near the center of the district at elevations below 4,200 m.

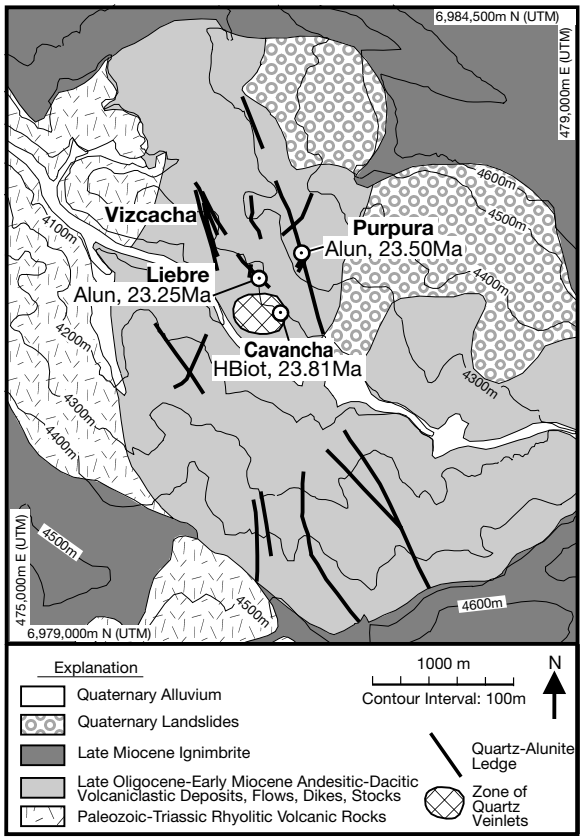

FIG. 10. Simplified district geology map of La Pepa. Based mostly on unpublished mapping by Compañia Minera Horus geologists. Shows $^{40}Ar/^{39}Ar$ dates and sample locations. Alun = alunite, H Biot = hydrothermal biotite.

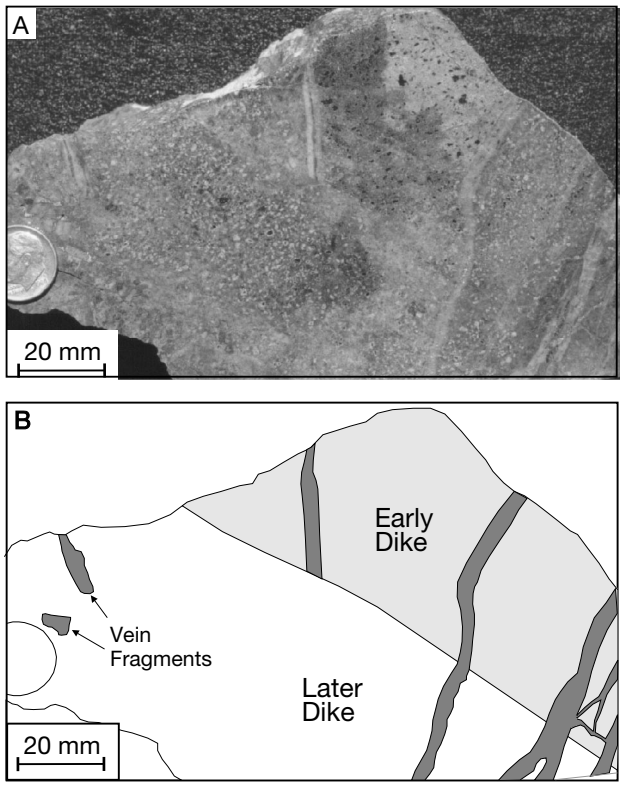

FIG. 11. Example of multiple cycle of intrusions and A-veinlets at the Cavancha deposit at La Pepa. A. Photograph. B. Explanantion. Early fine-grained feldspar porphyry dike with pervasive hydrothermal biotite was cut by an early A-veinlet. Later feldspar porphyry dike truncated the early A-veinlet. Note A-veinlet fragments in the dike. Dike was subsequently cut by a later set of A-veinlets. Hydrothermal biotite is variably overprinted by pyrite and clay resulting in the mottled appearance.

Gold grades are generally 0.5 to 1 ppm, and hypogene copper grades are <0.15 percent.

Quartz veinlets coincide with a zone where hornblende and some igneous biotite are replaced by fine-grained aggregates of hydrothermal biotite and magnetite. Biotitized rocks contain up to 2.5 vol percent magnetite. Commonly biotite and magnetite are partially replaced by chlorite and hematite, respectively. From depths of about 175 m and less, biotitized rocks are overprinted by sericite, albite, and clay. The total sulfide abundance increases from 1 to 2.5 vol percent to 3 to 6 vol percent, and pyrite/chalcopyrite ratios increase from ~1 to >50.

As at Cerro Casale, the sequence of intrusion, pervasive biotization, A-veinlets, and banded quartz veinlets appears to have repeated several times at Cavancha. A-veinlets and banded quartz veinlets cut dikes, dikes truncate sets of both veinlet types, and fragments of quartz veinlets are commonly seen in dikes and intrusive breccias (Fig. 11). Cavancha is the only deposit studied where A-veinlets locally cut banded quartz veinlets. Many quartz veinlets are hybrid A-banded quartz veinlets, sharing characteristics of both vein types.

D-veins at Cavancha cut all intrusions and all other quartz veinlets (Fig. 12). The veins are commonly vuggy and contain >50 vol percent pyrite with quartz and, locally, minor sericite. Thicker D-veins, up to 10 cm, locally contain several percent copper ± arsenic ± iron sulfide minerals as inclusions in pyrite, between pyrite grains, or in fractures that cut pyrite. Detailed study of one section revealed a temporal sequence of early chalcopyrite, then bornite + enargite, followed by late chalcopyrite + tennantite, all with pyrite. Native gold and calaverite occur in pyrite, commonly in close association with bornite. Local molybdenite and trace quantities of galena and cassiterite are also present. Two-meter intervals in drill core with thick D-veins commonly contain 1 to 3 ppm Au. A multielement analysis of one D-vein yielded concentrations of 12 ppm Au, 4.1 ppm Ag, 0.21 percent Cu, and 18.8 ppm Te (Table 3).

A ledge composed of vuggy residual quartz clearly postdates A-veinlets in drill core at Cavancha (Fig. 13). Pyrite fills the vugs and occurs in fractures, locally with minor chalcopyrite, zinc-bearing tennantite, sphalerite, and sericite.

High-grade epithermal gold ore in quartz-alunite ledges

Quartz-alunite ledges with high gold grades occur in volcanic rocks at elevations between 4,500 and 3,900 m and are locally within 100 m of the Cavancha deposit (Figs. 10, 14). Ledges range from a few centimeters to about 3 m in width, strike predominantly N 10° to 40° W, and most dip steeply. Strike lengths range up to several hundred meters, significantly greater than the ledges at Refugio and Aldebarán. High gold contents are confined mainly to ledges; gold grades

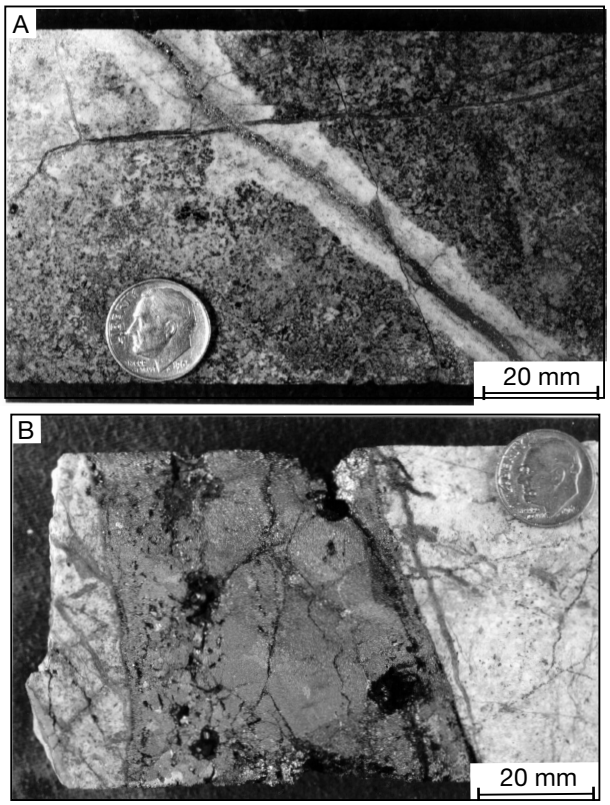

FIG. 12. Photographs of D-veins from the Cavancha deposit at La Pepa. A. D-vein with quartz-sericite-pyrite halo cutting and offsetting banded quartz veinlet. B. Example of thick, vuggy, gold-bearing D-vein cutting A-veinlets.

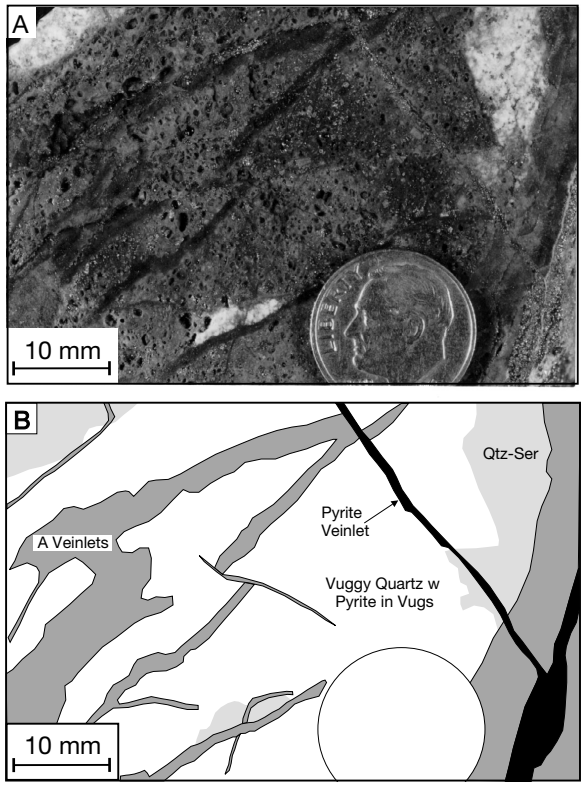

FIG. 13. A. Photograph of vuggy residual quartz from the Cavancha deposit at La Pepa that clearly postdates A-veinlets; otherwise, quartz associated with the A-veinlets would have filled the vugs in the vuggy quartz. B. Diagram illustrating features in the photograph. The vuggy quartz contains quartz, rutile, and pyrite but lacks advanced argillic indicator minerals such as alunite, pyrophyllite, kaolinite, or diaspore. Note pyrite that cuts across or fills open spaces in the vuggy quartz. Bleached zones are quartz-sericite.

are mostly <0.2 ppm outside the ledges. Grades are highest at intersections with north- to northeast-striking ledges. Ledges consist of quartz, alunite, pyrite, and rutile with local core zones of vuggy residual quartz. Ledges are flanked by a quartz-illite zone with 2 to 3 vol percent pyrite and <0.5 percent tourmaline. Illite appears to have partially replaced alunite at the ledge contact.

The ledges show strong vertical zonation that is best exhibited in the Purpura ledge system (Fig. 10). At elevations above about 4,360 m, rocks at the surface at Purpura are pervasively altered to quartz and kaolinite with minor quartz-alunite zones. Between 4,360 and 4,253 m elevation, ore was mined from ledges at Purpura that closely resemble the bulk of the ore mined from the Vizcacha and Liebre ledge systems (Fig. 10). Narrow veinlets of chalcedony with barite and minor alunite cut quartz-alunite and vuggy residual quartz and commonly occupy the centers of the ledge. Open spaces in vuggy quartz are lined with coarse-grained barite, clear, terminated quartz crystals, and minor enargite. About 5 vol percent pyrite occurs as disseminations in quartz, intergrowths with alunite, and as vug coatings.

Between the 4,253- and 4,243-m levels at Purpura, the amount of barite decreases abruptly and the ledges contain >5 vol percent pyrite and up to 25 vol percent enargite. Enargite occurs mainly in chalcedony veins and as vug coatings in vuggy quartz where it is locally intergrown with barite, pyrite, hypogene covellite, and alunite. Relative ages of the major minerals, on the basis of a sequence of veinlets found in one sample, is (1) alunite, (2) alunite + pyrite, (3) pyrite, and (4) chalcedony + enargite + pyrite. Alunite formation, therefore, mainly precedes but also overlaps in time with enargite deposition. According to mine geologists (A. Valverde, pers. commun., 1993), the main Purpura ledge narrows with depth and contains pyrite and chalcopyrite near the bottom of the workings, which were inaccessible at the time of this study.

$^{40}Ar/^{39}Ar$ Geochronology

Objectives

Field evidence indicates that quartz-alunite ledges are younger than quartz veinlets and hydrothermal biotite at Refugio and La Pepa (Table 1). In order to obtain quantitative information on time differences between the epithermal (alunite) and porphyry (biotite) environment, we conducted a reconnaissance ^{40}Ar-^{39}Ar study. Such information can be used to address the question of genetic links between these two environments, on the basis of recent studies of the longevity of porphyry systems. Attempts to define the duration of magmatic-hydrothermal systems related to porphyry-copper

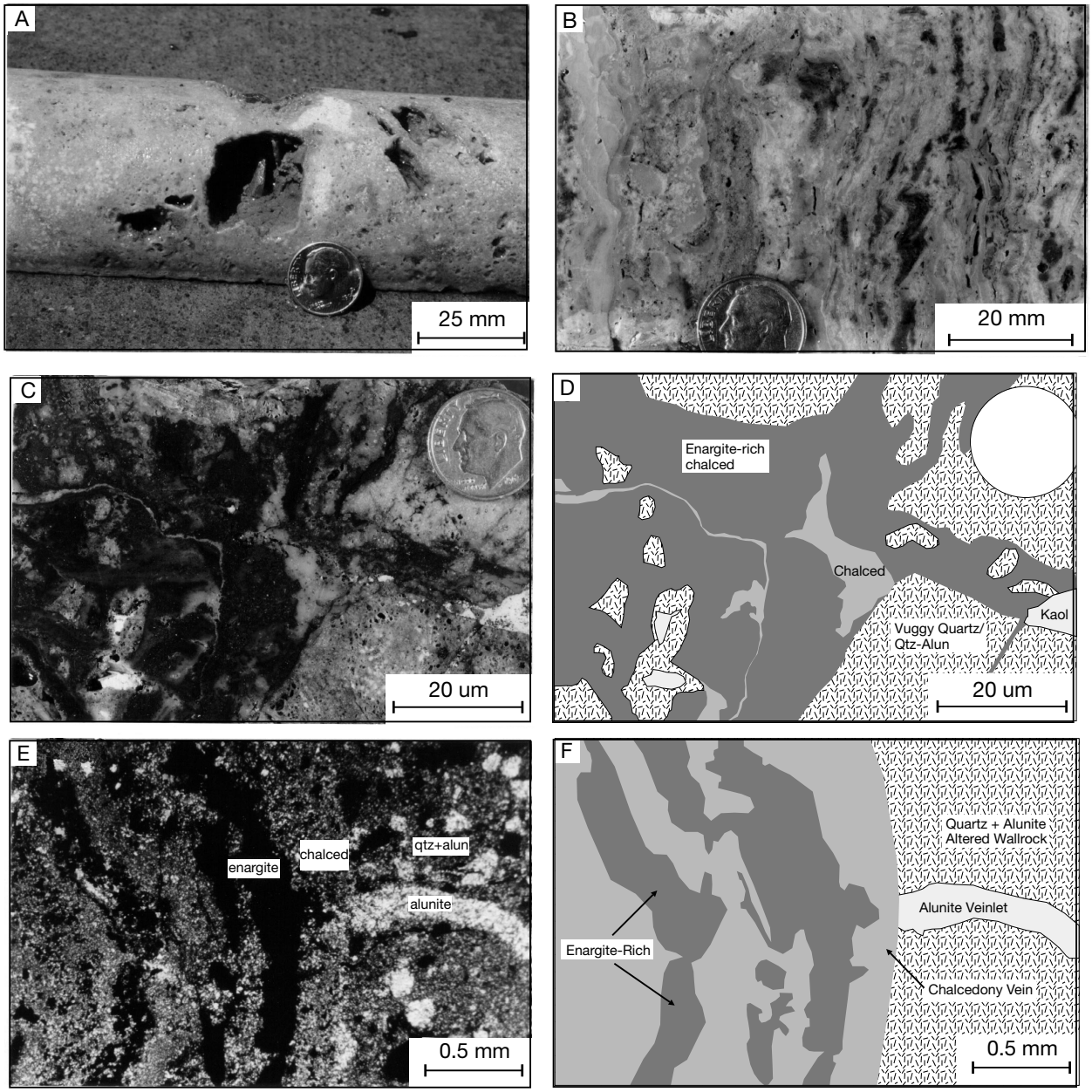

FIG. 14. High-grade samples from La Pepa. A. Photograph of core sample that assayed 299 ppm gold from the main Liebre ledge; it shows quartz-alunite with erratically developed vuggy quartz. Note coarse barite crystals in large vugs. Micron-sized native gold and calaverite occur as inclusions in pyrite. A native gold grain was found lining a vug in vuggy quartz. However, the free milling characteristics of the ore suggest that relatively coarse-grained gold may have been plucked from fractures and vugs during preparation of polished thin sections. B. Photograph of sample from the Purpura ledge system showing open-space textures of interlayered enargite-rich and enargite-poor chalcedony with minor alunite. C. Photograph. D. Explanation. Enargite-rich sample from the Purpura ledge system. Enargite-rich chalcedony (chalced) cuts and occurs as matrix to brecciated quartz-alunite altered rock with erratically developed vuggy quartz. Enargite locally contains inclusions of calaverite and Hg tellurides. Enargite-poor chalcedony crosscuts enargite-rich chalcedony. Late kaolinite (kaol) occurs in cavities. E. Photomicrograph (crossed polars). F. Explanation. Chalcedony with enargite cuts alunite veinlet in wall rock altered to quartz-alunite-pyrite-rutile, from the Purpura ledge system. qtz-alun = quartz-alunite.

deposits have been based on a combination of techniques, including U-Pb, ^{40}Ar-^{39}Ar, and Re-Os, that yield higher precision than the older K-Ar technique. Such studies indicate durations of about 1 m.y. (Dilles and Wright, 1988; Parry et al. 1998; Watanabe et al., 1999; Gustafson et al., 2001) to <400,000 years (Arribas et al., 1995; Marsh et al., 1997), excluding precursor equigranular stocks. Therefore, time gaps of less than 1 m.y. are taken here as highly suggestive of a genetic link between the porphyry and epithermal environment, whereas time gaps >1 to 2 m.y. would suggest no genetic connection. We apply this test to hydrothermal biotite (three samples) and alunite (four samples), dated from Refugio

(Pancho deposit), Aldebarán, and La Pepa. In addition, two igneous biotite samples were dated from the Verde orebody at Refugio. The dates are summarized in Figure 15 and Table 4. Uncertainties for all ages are quoted at the 2σ confidence level. Sample descriptions, locations, and preparation, analytical and calculation procedures are found in the Appendix.

Interpretation of the Refugio $^{40}Ar/^{39}Ar$ data

The weighted mean age calculated for a sample of hydrothermal biotite from Pancho (LYR-3 45-50m) is 23.22 ± 0.06 Ma (Figs. 6, 16A). The apparent age spectrum for an alunite sample from Pancho (RP030) does not have any interpretable plateau-like segments and is considered disturbed (Fig. 16B). The isochron failed the mean square of weighted deviates (MSWD) test and is not considered reliable. The ages determined from spectra for igneous biotite from the late quartz diorite porphyry stocks at Verde West (23.27 ± 0.06 Ma, RV050; Figs. 6, 16C) and Verde East (23.28 ± 0.06 Ma, RV078; Figs. 6, 16D) are indistinguishable from the age of hydrothermal biotite at Pancho and a K-Ar date of 22.8 ± 1.2 Ma (2σ) by Sillitoe et al. (1991) on igneous biotite from an unaltered dacite dome south of Verde. The dates are consistent with a short duration for intrusions and porphyry-style mineralization in the Refugio district.

Interpretation of the Aldebarán $^{40}Ar/^{39}Ar$ data

A weighted mean plateau age of 13.89 ± 0.04 Ma for hydrothermal biotite from the late biotite porphyry at Cerro Casale (ALC-1 158-159m; Figs. 8, 16E) is indistinguishable from a weighted mean age of 13.91 ± 0.04 Ma determined for alunite from a ledge west of Cerro Casale (AVZ005; Figs. 8, 16F). This suggests that alunite is genetically linked with potassic alteration and porphyry-style mineralization. The biotite and alunite dates are indistinguishable from the 13.5 ± 1.0 Ma (2σ) K-Ar date on alunite obtained from a ledge on Cerro Catedrál (Sillitoe et al., 1991). Given the large uncertainty attached to the K-Ar date, alunite at Cerro Catedrál

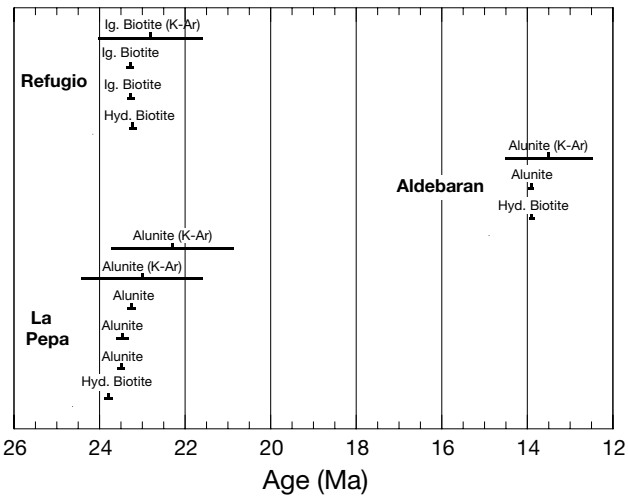

FIG. 15. Summary of preferred $^{40}Ar/^{39}Ar$ ages and uncertainties (2σ) from Table 4 and K-Ar dates published by Sillitoe et al. (1991). Hyd. Biotite = hydrothermal biotite, Ig. Biotite = igneous biotite.

TABLE 4. Summary of $^{40}Ar/^{39}Ar$ Age Data

District	Sector	Sample	Mineral	Weighted mean plateau age (Ma ± 2σ)[1]	Weighted mean age (Ma ± 2σ)[2]	Inverse isochron age (Ma ± 2σ)[3]	Isochron-derived MSWD[4]	40/36 ratio (± 2σ)
Refugio	Pancho	LYR-3 45-50m	Biotite		23.22 ± 0.06[5]	23.42 ± 0.58	3.54 < (3.83)	280.6 ± 45.0
Refugio	Pancho	RP030	Alunite	Disturbed	Disturbed	22.69 ± 0.82	49.92 > (2.63)	290.4 ± 21.4
Refugio	Verde West	RV050	Biotite	23.27 ± 0.06[5]		23.19 ± 0.14	0.29 < (2.41)	310.3 ± 18.4
Refugio	Verde East	RV078	Biotite		23.28 ± 0.06[5]	23.31 ± 0.46	1.92 < (3.83)	288.1 ± 139.8
Aldebarán	Cerro Casale	ALC-1 158-159m	Biotite	13.89 ± 0.04[5]		13.89 ± 0.06	0.38 < (2.41)	313.1 ± 3.4[6]
Aldebarán	Vein zone	AVZ005	Alunite		13.91 ± 0.04[5]	13.98 ± 0.10	0.14 < (3.00)	292.4 ± 2.8
La Pepa	Cavancha	CAV-2 258-264m	Biotite		23.81 ± 0.08[5]	23.88 ± 0.12	0.86 < (2.63)	291.5 ± 3.8
La Pepa	Purpura vein	LP004W	Alunite		23.50 ± 0.06[5]	23.39 ± 1.14	2pt isochron	319.0 (2 pt isochron)
La Pepa	Liebre vein	CAV-4 41.5mA	Alunite		23.47 ± 0.12[5]	(1 step)	(1 step)	(1 step)
La Pepa	Liebre vein	CAV-4 41.5mB (replicate analysis)	Alunite	23.25 ± 0.08[5]		23.26 ± 0.16	0.07 < (3.83)	295.5 ± 1.0

All ages calculated using constants recommended by Steiger and Jäger (1977)

[1] Passes the criteria of Lanphere and Dalrymple (1978) for a plateau age; explanation of how the weighted mean and uncertainty were calculated is explained in the Appendix and detailed in Muntean (1998)

[2] Meets only two of the three the criteria of Lanphere and Dalrymple (1978) for a plateau age; explanation of how the weighted mean and uncertainty were calculated is explained in the Appendix and detailed in Muntean (1998)

[3] Isochron age determined by graphing the temperature steps from the plateau or plateau-like segment on a $^{36}Ar/^{40}Ar$ versus $^{39}Ar/^{40}Ar$ plot

[4] MSWD: mean square of weighted deviates, a goodness-of-fit statistic (York, 1969); if the value is less than the value in the parenthesis, the data are linearly correlated and represent an isochron; can be calculated only for three or more points.

[5] Ages used in the interpretation discussed in the text

[6] Significantly different at the 95% confidence level than the atmospheric ratio of 295.5; the ratio of 313.1 was used in the age calculations

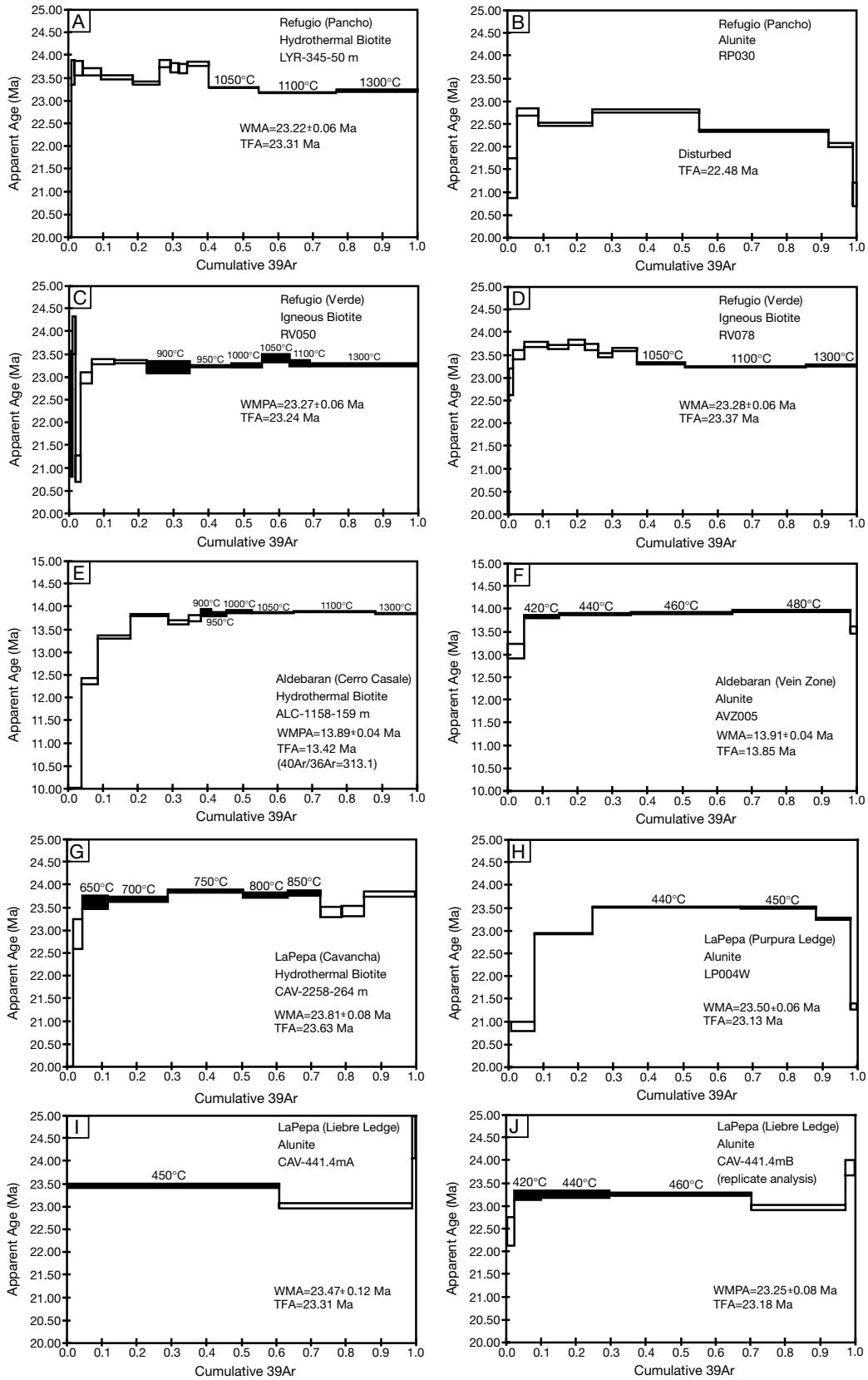

FIG. 16. Apparent $^{40}Ar/^{39}Ar$ age spectra. The error bars in the spectra correspond with $\pm 1\sigma$ without considering the error in J. The shaded steps are the temperature steps used in the age determination. TFA = total fusion age, WMA = weighted mean age ($\pm 2\sigma$); WMPA = weighted mean plateau age ($\pm 2\sigma$).

could be related to the intrusive center at Cerro Casale or a separate intrusion under Cerro Catedrál .

Interpretation of the La Pepa $^{40}Ar/^{39}Ar$ data

The apparent age spectrum for a hydrothermal biotite sample at the Cavancha deposit at La Pepa resulted in a weighted mean age of 23.81 ± 0.08 Ma (CAV-2 258-264m; Figs. 10, 16G). The date represents a minimum age for potassic alteration and porphyry-style mineralization at Cavancha.

A weighted mean age of 23.50 ± 0.06 Ma was calculated from a plateau-like segment for an alunite sample from the Purpura ledge (LP004W; Figs. 10, 16H). Two replicate analyses of an alunite sample from the Liebre ledge resulted in similar patterns of apparent age spectra. In the first analysis, 99 percent of the ^{39}Ar was released in two discordant steps (CAV-4 41.5 mA, Fig. 16I). The sample was analyzed before the temperature range at which argon is released from alunite was confidently established. A weighted mean plateau age of 23.25 ± 0.08 Ma was calculated for a duplicate analysis (CAV-4 41.5 mB; Figs. 10, 16J). On the basis of the similar patterns of the two replicate spectra, the first step of the first analysis (CAV-4 41.5 mA) is considered to be analogous to the plateau of the second analysis.

All three alunite ages are significantly younger than the biotite age at the 95 percent confidence level. K-Ar dates on alunite from La Pepa, 23.0 ± 1.4 Ma and 22.3 ± 1.4 Ma (2σ) (Sillitoe et al., 1991), are also younger than the biotite, although only one date is younger at the 95 percent confidence level. Given the ages interpreted from the apparent age spectra and estimated 2σ uncertainties, the time interval between cooling of hydrothermal biotite through its blocking temperature and the formation of alunite appears to be at least 140,000 years and possibly as great as 720,000 years. Even if we take the estimated uncertainties of the weighted mean ages calculated from the apparent age spectra to be too low, the ages and uncertainties derived from isochrons also indicate that the age of alunite is statistically distinct from the age of secondary biotite. The isochron ages suggest a time gap of at least 340,000 years to as great as 900,000 years (using the CAV-4 41.5mB analysis). Thus, biotite and alunite at La Pepa have ages that pass our "criteria" for being cogenetic on the system scale.

Although cogenetic on the system scale, the apparent time gap of at least 140,000 years between hydrothermal biotite and alunite contains implications for the evolution of hydrothermal fluids in the La Pepa system. Given that magmatic-hydrothermal alunite forms mostly between 200° to 300°C in high-sulfidation epithermal deposits (Arribas, 1995), and that the blocking temperature of biotite is about 300ºC (see Appendix), the simplest explanation is that little cooling took place during the time gap and that the alunite represents the end stage of the system that formed the biotite. The apparent isothermal conditions that lasted for at least 140,000 to as great as possibly 900,000 years might be explained by intrusions that are deeper and later than the exposed, biotized intrusions.

Discussion and Conclusions

Summary of early mineralization

Early mineralization is defined as the period of hydrothermal activity that occurred before cessation of intrusive activity at present levels of exposure (Table 5). Potassic alteration

TABLE 5. Characteristics of Early Mineralization

Deposit	Tonnage (million metric tonnes)	Gold grade (ppm)	Hypogene copper grade (%)	Copper %/ gold (ppm)	K silicate assemblages	A-veinlets	Banded quartz veinlets	Propylitic assemblages	Magnetite + hematite (vol %)	Total sulfide (vol %)
Verde[1] (Refugio)	101	0.88	0.03	0.03	Absent	Absent	Abundant	Central	1–4	<1
Pancho[2] (Refugio)	68	0.96	0.1	0.1	Central mag-ksp-olig out to bio-mag	Moderate, lower levels	Abundant	Peripheral	2–5	<1
Cavancha[3] (La Pepa)	n.a.	1	0.1	0.1	Bio-mag	Moderate	Moderate	Absent?	<2.5	<2.5
Cerro Casale[4] (Aldebarán)	1,114	0.71	0.26	0.37	Deep, central ksp-mag/spec out to bio-mag	Abundant, lower levels	Minor, higher levels	Peripheral	4–7	<1

Abbreviations: bio = biotite, ksp = K feldspar, mag = magnetite, olig = oligoclase, spec = specular hematite; n.a. = not available

[1] Verde: tonnes and gold grade are mineable reserve (Brown and Rayment, 1991); copper grade from Flores (1993)

[2] Pancho: tonnes and gold grade are inferred resource (Brown and Rayment, 1991); copper grade is crude estimate based on inspection of samples and drill hole assays

[3] Cavancha: gold and copper grades are crude estimates based on inspection of drill hole assays

[4] Casale Hill: tonnes, gold grade, and copper grade are measured and indicated resource (R. Pease, pers. commun., 2000)

zones and A-veinlets are absent at Verde but are strongly developed at Cerro Casale. In contrast, banded quartz veinlets are dominant at Verde and occur only on the periphery and in upper levels of Cerro Casale. The Pancho and Cavancha porphyry deposits show characteristics of both Verde and Cerro Casale. Thus, we have defined a spectrum of porphyry-type deposits ranging from the Cerro Casale porphyry gold-copper deposit, which shares many characteristics of porphyry copper deposits worldwide, to Verde, characterized by banded quartz veinlets that appear to be an essential characteristic of porphyry gold deposits. Pancho and Cavancha are telescoped systems in which banded quartz veinlets overprinted potassic alteration zones and A-veinlets. Verde and Cerro Casale may occupy a greater vertical extent. We speculate that banded quartz veins may have been eroded from the top of Cerro Casale and that A-veinlets accompanied by higher copper/gold ratios may underlie Verde.

Of the deposits studied, Cerro Casale displays the highest hypogene copper/gold ratios (percent Cu/ppm Au = 0.38), placing it in the porphyry gold-copper category (Sillitoe, 2000). Verde has the lowest copper/gold ratios (ca. 0.03), whereas Pancho and Cavancha have intermediate ratios (ca. 0.1). With the exception of La Pepa, total sulfide content is generally <1 vol percent for early mineralization. Average magnetite and hematite content ranges from as high as 7 vol percent at Cerro Casale, a value at the higher end of many gold-rich porphyry copper deposits (cf. Sillitoe, 1979), to as low as 1 to 4 vol percent at Verde.

Summary of late mineralization

Late mineralization is defined as the period of hydrothermal activity that occurred after cessation of intrusive activity at present levels of exposure (Table 6). D-veins serve as the time line signifying the initiation of late mineralization, because at Pancho, Cavancha, and Cerro Casale, no intrusions, A-veinlets, or banded quartz veinlets cut D-veins.

Pervasive pyrite-albite-clay assemblages occur on the periphery and/or at the higher levels of each deposit and are most intense at the Cavancha deposit at La Pepa. This alteration style may have formed contemporaneously with early mineralization; however, in areas of spatial overlap, pyrite-albite-clay assemblages overprint potassic assemblages. Total sulfide content, mostly as pyrite, ranges from 2 to 6 vol percent. Quartz-alunite ledges are widespread in all of the districts. Barren quartz-alunite ledges at Aldebarán formed during early porphyry mineralization. In contrast, gold-bearing ledges at La Pepa postdated porphyry-style mineralization by a few 100,000 years.

Formation of porphyry-style mineralization

Our interpretation of the temporal and spatial development of magmatic-hydrothermal systems in the districts studied here is presented in the time-space diagram of Figure 17. Pancho, Cerro Casale, and Cavancha developed similarly: intrusion of porphyry was followed by pervasive potassic alteration and formation of A-veinlets and was terminated by banded quartz veinlets. In contrast, Verde underwent repeated cycles of intrusion followed by formation of banded quartz veinlets, without A-veinlets and potassic alteration. Alteration-mineralization events were repeated in numerous cycles in each deposit, but their intensity was not the same in all cycles. Parts of the early quartz diorite porphyry stocks at the Pancho and Cerro Casale deposits lack potassic assemblages or A-veinlets, suggesting that fluid flux during these early stages was minimal. Age relations presented above indicate that the bulk of the A-veinlets formed and copper-gold mineralization took place during intrusion of porphyry dikes. Only minor mineralization was associated with the latest intrusions as exemplified by the late quartz diorite porphyry plugs at Verde and the biotite porphyry at Cerro Casale. These late intrusions could represent a deep magma source that was depleted in volatiles, metals, and sulfur by earlier intrusive events (cf. Gustafson and Hunt, 1975; Clode et al., 1999).

We favor a model whereby a supercritical NaCl-bearing aqueous fluid at depths of >6 km and temperatures >800°C ascends along a quasi-adiabatic path (path 1a, Fig. 18) as supported by critical phase inclusions below some porphyry deposits (cf. Bodnar, 1995). This fluid encounters the two-phase field at depths of ~5 to 6 km and separates into a high-density liquid and a low-salinity vapor (Sourirajan and Kennedy, 1962; Bodnar et al., 1985; Pitzer and Pabalan, 1986; Fournier, 1999). The liquid and vapor ascend with the magma and permeate into fractures along dike margins. Fluid inclusion data

TABLE 6. Characteristics of Late Mineralization

Deposit	Pyrite-albite-clay assemblages	D-veins	Total sulfide[1] (vol %)	Quartz-alunite ledges
Verde (Refugio)	Peripheral	Absent	2–4	qtz-alun, <1ppm Au
Pancho (Refugio)	Peripheral, higher levels	Very minor	2–4	qtz-alun, <1ppm Au
Cavancha (La Pepa)	Widespread, higher levels	Moderate (Au-bearing)	3–6	(District) qtz-alun/vuggy qtz/chal; local high grade Au-(Cu)
Casale Hill (Aldebarán)	Peripheral, higher levels	Moderate; local polymetallic veins	2–4	(District) qtz-alun, local vuggy qtz; mostly <1ppm Au

Abbreviations: alun = alunite, chal = chalcosite, qtz = quartz

[1] Total sulfide refers to zones of pervasive pyrite-albite-clay assemblages with or without D-veins; it does not include quartz-alunite ledges

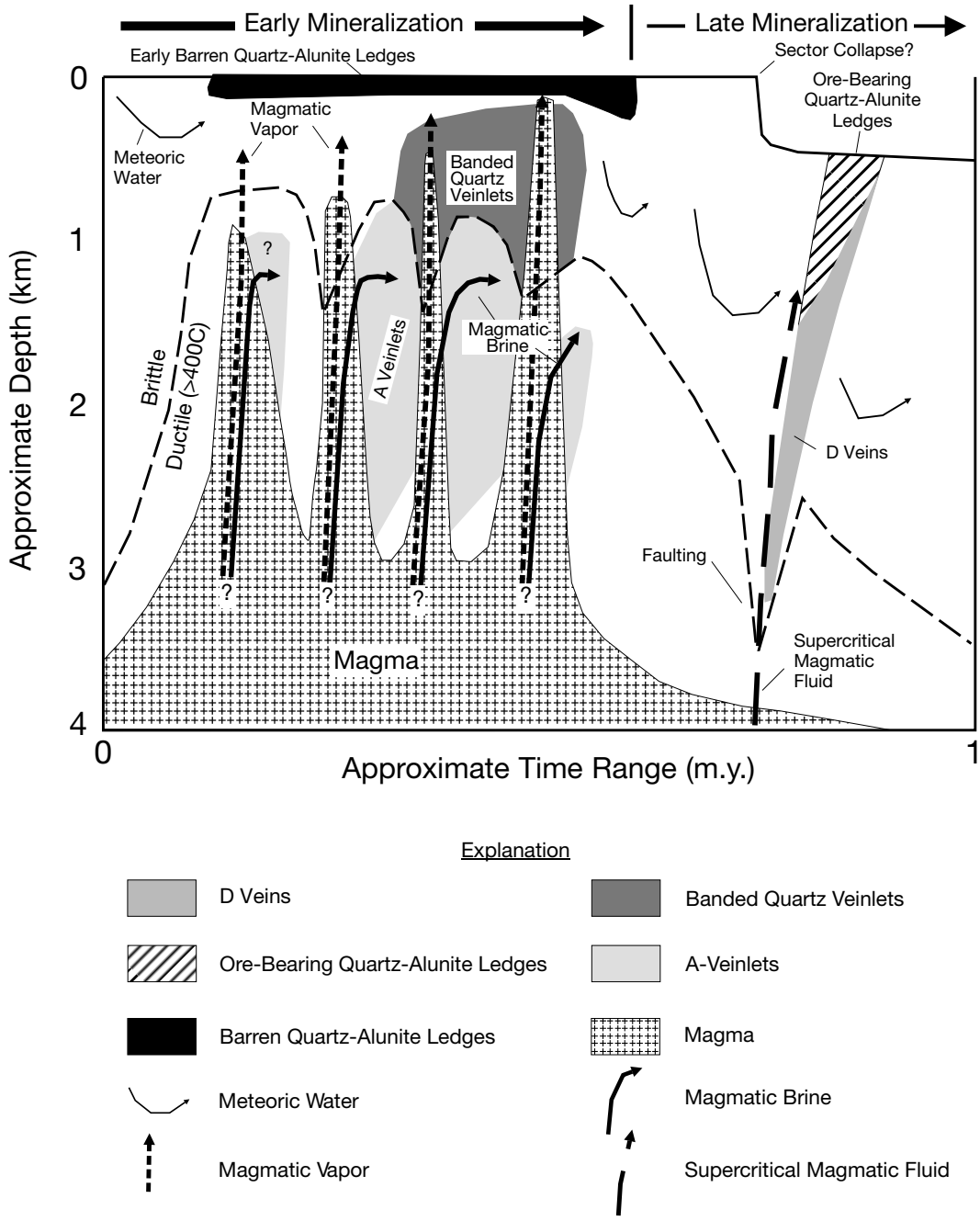

FIG. 17. Time-space diagram for typical magmatic-hydrothermal system in the Maricunga belt.

from A-veinlets indicate temperatures at this stage were close to 700°C.

The ductile-brittle transition is depicted in Figure 17 as rising to near-surface levels as each intrusion is emplaced. With time, as the intrusions cool, the transition retreats gradually to greater depths, but it retreats abruptly during high strain-rates accompanying dike emplacement. At temperatures above about 400°C and strain rates less than 10^{-14}/s, rock of quartz diorite composition behaves quasiplastically, making brittle fracture difficult and allowing fluid pressures to approach lithostatic values (Fournier, 1991, 1999). Fractures that form during release of fluid overpressures at depth would quickly seal as strain rates decrease and as quartz precipitates owing to pressure release (Fournier, 1985, 1999). The restriction of A-veinlets and potassic assemblages to intrusive rocks at Pancho, Cerro Casale, and Cavancha indicates that the high density of the hypersaline liquid combined with low permeability of the stocks results in trapping of the liquid within crystallized portions of the intrusions. Between intrusive events, the liquid cools isobarically, and fractures remain open for longer

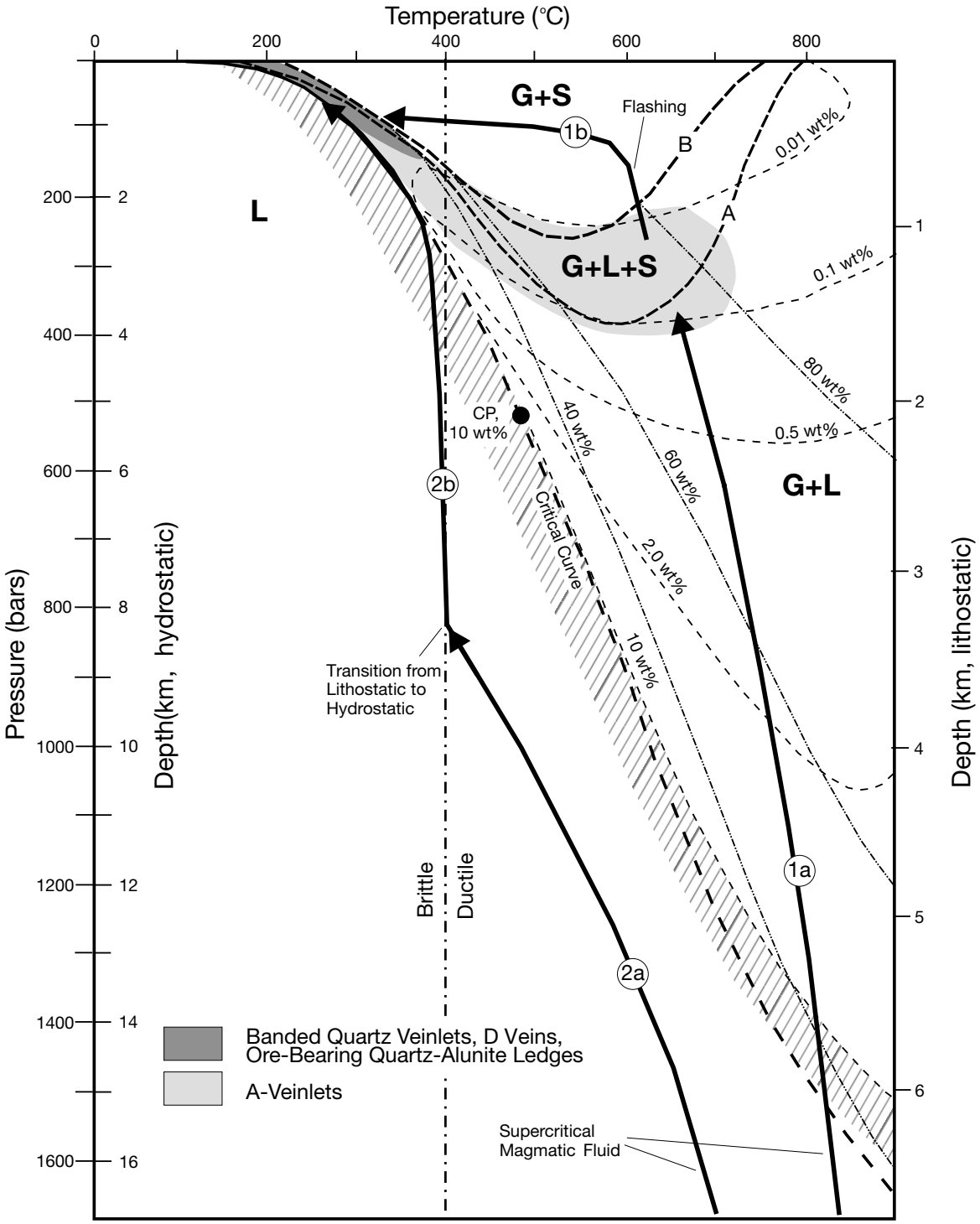

FIG. 18. Phase relations in the NaCl-H_2O system. Based on data of Bodnar et al. (1985) and Pitzer and Pabalan (1986) (after Fournier, 1987, 1999). Depths assuming a 1g/cm^3 hydrostatic load and a 2.5g/cm^3 lithostatic load are also shown. Isopleths of NaCl in liquid and in gas in the two-phase gas + liquid field are shown by the dash and double-dot lines and short, lightweight dashed lines, respectively. Dashed curve A shows the three-phase boundary, G + L + S, for the system NaCl-H_2O; dashed curve B is the liquid saturation curve for the NaCl-KCl-H_2O system where Na/K ratios in the solution are fixed by equilibration with albite and K feldspar at the indicated temperatures. Uncertainties, probably on the order of 100 to 200 bars, are associated with the projections of the isopleths of NaCl in liquid into the three-phase field, G + L + S. The hachured region accentuates the boundary between the one-phase liquid fluid with a salinity of 10 wt percent and the two-phase liquid + gas field. The vertical dot-dash line shows the approximate temperature of the brittle-ductile boundary when the strain rate is 10^{-14} s^{-1}. The paths labeled 1a, 1b, 2a, and 2b refer to the proposed fluid paths responsible for the formation of A-veinlets (light gray region), banded quartz veinlets, D-veins, and ore-bearing quartz-alunite ledges (dark gray region) as explained in the text. CP = critical point, G = gas, L = liquid, S = solid salt.

periods of time. Therefore, with time for each intrusive event, A-veinlets become wider and more continuous. This process repeats with each subsequent intrusive event; the more continuous A-veinlets of earlier stages are truncated by intrusions and crosscut by discontinuous, irregular A-veinlets of later stages.

As proposed by Muntean and Einaudi (2000), banded quartz veinlets formed during rupturing of the brittle-ductile boundary at low pressures, a process that led to flashing of high-density liquid and vapor to vapor + salt (path 1b, Fig. 18). The ruptures were probably caused by increased strain rate accompanying intramineral intrusions. Assuming a two-component NaCl-H_2O system and equilibrium with a vapor phase, temperatures and salinities derived from fluid inclusion data indicate pressures between 200 and 400 bars for A-veinlets, corresponding to depths of 0.8 to 1.6 km under lithostatic pressure (Fig. 18). Temperatures and salinity estimates for the banded quartz veinlets indicate similar to more shallow depths of about 0.2 to 1.5 km under hydrostatic pressures of 10 to 150 bars (Fig. 18; Muntean and Einaudi, 2000), consistent with the zonal position of banded quartz veinlets above A-veinlets. Muntean and Einaudi (2000) suggested that if sulfur were lost to the vapor phase during flashing, precipitation of iron and iron-copper sulfides would have been inhibited, resulting in deposition of gold and magnetite. Precipitation of late calcite, chlorite, K feldspar, pyrite, and additional gold in the banded veinlets suggests the presence of near-neutral pH fluids that may have originated from the earlier loss of acid volatiles such as HCl, CO_2, and H_2S during flashing.

Formation of high-sulfidation epithermal mineralization

Most genetic models for high-sulfidation epithermal deposits stress an early stage of quartz-alunite ledge formation associated with low-salinity vapors and followed by a later ore-forming stage associated with higher-salinity liquid (see summary by Arribas, 1995). The early stage is linked to processes occurring at depth during evolution of coexisting magmatic vapor and hypersaline liquid. The liquid cools isobarically at depth, resulting in potassic alteration and sulfide precipitation. Because of its lower density and hence viscosity, the vapor phase preferentially escapes the intrusion across the ductile-brittle transition (steep dashed paths, Fig. 17). Vapor, where focused upward along structures, either discharges directly as fumaroles or condenses into meteoric water. The resulting highly reactive fluid leaches the rock and forms quartz-alunite ledges. Such ledges have only slightly anomalous metal values because of the limited metal-transporting capacity of low-pressure, low-salinity vapors (Krauskopf, 1957, 1964; Hedenquist et al., 1994; Hedenquist, 1995). This model is supported in part by the studies of Arribas et al. (1995) at Lepanto-Far Southeast and by our studies at Aldebarán, where alunite formed synchronously with hydrothermal biotite.

Further support for the above model and evidence bearing on the nature of hydrothermal fluids linked to ore deposition in the epithermal environment is found in the study of Lepanto-Far Southeast by Hedenquist et al. (1998). Gold-copper ore deposition in the Lepanto high-sulfidation epithermal deposit postdated potassic alteration in the underlying Far Southeast porphyry copper-gold deposit. Fluid inclusions in enargite and stable isotope data from Lepanto (Mancano and Campbell, 1995; Hedenquist et al., 1998) and other high-sulfidation epithermal deposits (Deen et al., 1994; Arribas et al., 1995) indicate the presence of magmatic fluids, variably diluted by meteoric water, resulting in salinities between 0.2 and 20 wt percent NaCl. Most present data are inconsistent with a low-salinity vapor as the fluid source of metals (cf. Sillitoe, 1983; Heinrich et al., 1999), but they are consistent with a metal source associated with deep, supercritical magmatic fluids (Hedenquist et al., 1998).

Alternatives to the above scenario are suggested by our data from La Pepa, where quartz-alunite ledges formed at least 140,000 years to as much as 900,000 years after hydrothermal biotite in the porphyry. Although gold-enargite-barite ore at La Pepa cuts quartz-alunite and vuggy quartz (Fig. 14), ore is everywhere enveloped by quartz-alunite, strongly suggesting that ore and alteration products formed from the same fluid, following the concept of ubiquitous concentricity (Meyer and Hemley, 1967). As a variation on the theme developed by Hedenquist et al. (1998), we propose that both gold-enargite-barite ore and enveloping quartz-alunite at La Pepa formed at essentially the same time from a late, supercritical magmatic fluid that cooled and eventually boiled upon ascent. Although stable isotope and quantitative fluid inclusion data are lacking, the field evidence, the radiometric dates, and the fluid inclusion assemblage in quartz associated with enargite in ledges at La Pepa are consistent with such a view.

This alternative scenario requires the ascending, supercritical magmatic fluid to cool below its critical temperature without entering the two-phase liquid + vapor field (path 2a, Fig. 18). The fluid crossed the brittle-ductile boundary at 400°C and 3 to 4 km depth at lithostatic pressure (Figs. 17, 18), below the critical temperature for a fluid with a salinity of 10 wt percent NaCl, a salinity considered appropriate for supercritical magmatic fluids (cf. Hedenquist et al., 1998). Upon crossing into the brittle regime the liquid underwent abrupt decompression and boiled under hydrostatic pressure along the two-phase liquid + vapor curve at depths of about 2 to 3 km (path 2b, Fig. 18). Unlike phase separation above the critical temperature in the two-phase liquid + vapor field, boiling along the liquid + vapor curve below the critical temperature did not generate a hypersaline liquid but caused a progressive and moderate increase in the salinity of the liquid phase (Fournier, 1987). Upon cooling and boiling, disassociation of H_2SO_4, HCl, and other strong acids in the liquid, and the condensation of acid magmatic volatiles (e.g., SO_2, HCl) into shallow meteoric water above the ascending liquid resulted in sericitic alteration at depth and quartz-alunite and vuggy quartz near the surface (cf. Hemley et al., 1969; Hemley and Hunt, 1992). Ore was deposited from the liquid phase but, in contrast to the model of Hedenquist et al. (1998), broadly at the same time as quartz-alunite and vuggy quartz alteration (Fig. 17, Late mineralization).

Exploration applications

Our study has application mainly to exploration for porphyry gold deposits and related epithermal gold ore in the Maricunga belt. Our conclusions may have fewer applications to exploration programs in other regions.

Mapping the distribution and abundance of different quartz vein-types, in particular banded quartz veinlets, rather than simply the distribution of quartz veins, is fundamental in predicting copper/gold ratios and gold grades (e.g., Fig. 4; see also Muntean and Einaudi, 2000). Mapping of A and B quartz-veinlet distributions in many porphyry copper-gold deposits can successfully delineate the zones of best hypogene grades, such as at El Salvador, Chile (Gustafson and Hunt, 1975, p. 904); at Batu Hijau, Indonesia (Irianto and Clark, 1995, p. 303; Clode et al., 1999); and at Bingham, Utah (P. Redmond and M.T. Einaudi, unpub. data, 1998). However, this approach loses the hoped-for definition in some deposits of the Maricunga belt. The Pancho deposit is a particularly good example of this potential problem, in that the highest gold contents are not coincident with the quartz vein zone as a whole, but correlate with the younger, banded quartz vein portion of the pattern. At several of the deposits studied here, potassic assemblages and A-veinlets occur at lower elevations than banded veinlets, providing a vertical component to the use of mineralogy and vein type as vectors toward the best targets.

Banded quartz veinlets tend to occur in prominent subparallel arrays, as at Marte (Vila et al., 1991, p. 1279), and in arrays with radial distribution, as at Verde (Muntean and Einaudi, 2000, Figs. 6, 9). As a result, maps of veinlet attitudes can be used to predict the patterns and trends of gold grade. This study complements many other studies (e.g., Gustafson and Hunt, 1975, fig. 28; Carten et al., 1988, fig. 11) that have demonstrated that porphyry-type deposits typically contain systematic vein attitudes that are pluton-centered rather than regional in origin. This observation emphasizes the importance of structural mapping of veinlets in the evaluation of porphyry prospects. The term "stockwork" should receive less emphasis, conceptually and in practice, because of its implications of randomness.

The use of patterns of alteration styles in exploration for porphyry-type deposits is well established (e.g., Lowell and Guilbert, 1970) and has been recently discussed (Sillitoe, 2000). Here we simply stress that the model of porphyry-style alteration, especially if the presence of hydrothermal biotite is considered a requisite part, is not applicable to all porphyry gold deposits in the Maricunga. For example, potassic assemblages are not present at Verde. Banded quartz veinlets do not appear to have any temporally associated alteration, and their host rocks may appear relatively fresh. Some might conclude that Verde is not a porphyry-type deposit, but this conclusion would reflect an over-reliance on rigid descriptive models rather than insight that is of practical use.

Assessing whether quartz-alunite ledges can be economic targets for epithermal gold ore in the Maricunga belt and elsewhere is challenging. Insight might be gained, however, by contrasting the field observations of productive ledges at La Pepa with those of subeconomic ledges at Refugio and Aldebarán. The ledges at La Pepa have stronger preferred orientation and greater strike lengths, and they probably extend to greater depth than those at Refugio and Aldebarán (compare Fig. 10 with Figs. 6 and 8). These features may reflect the tapping of deeper fluids at La Pepa. The ledges at La Pepa have the best developed and most widespread vuggy residual quartz. Vuggy quartz is absent at Refugio and only locally present at Aldebarán. Restriction of most high-grade zones to vuggy quartz reflects the brittle nature and, thus, good permeability of vuggy quartz. The ledges at La Pepa have the most introduced chalcedony, quartz, barite, and enargite (commonly oxidized to scorodite), which fill fractures and line vugs. Except for rare barite, such introduced minerals are absent at Refugio and occur in much lesser amounts at Aldebarán. Although the relationship between D-veins and ledges has not been documented, the Cavancha porphyry system at La Pepa has the thickest D-veins with the highest gold grades. D-veins are absent at Verde, are rare at Pancho, and are narrower and have lower grades at Cerro Casale. Shallow, high-grade, barite-rich ores at La Pepa show a transition downward to lower grade enargite-rich ores. The same vertical zonation also occurs at Aldebarán, where, in addition, a native sulfur zone occurs above barite-bearing ledges.

Acknowledgments

We thank the personnel of Compañia Minera Maricunga, Amax Gold, and Bema Gold for funding the field portion and part of the analytical costs of this study, and we acknowledge in particular Neil Muncaster, Albert Brantley, and Roman Flores. We appreciate that Kinross Gold Corporation and Placer Dome permitted this research to be published. We also thank Compañia Minera La Pepa and Compañia Minera Newmont for access to the La Pepa property and its data. A large portion of this research was funded by National Science Foundation grant EAR9418301 awarded to M.T.E. We are grateful to Michael McWilliams for use of the $^{40}Ar/^{39}Ar$ laboratory at Stanford and his help in the interpretation of the $^{40}Ar/^{39}Ar$ results, and to Timothy Marsh for his insights on mineral separations and $^{40}Ar/^{39}Ar$ dating. We acknowledge Jim Reynolds of Fluid Inc. for numerous discussions on fluid inclusions and reviews of earlier versions of this manuscript. Formal reviews by Richard Sillitoe, Rod Kirkham, and Jeffrey Hedenquist helped us to express our thoughts more clearly and systematically. Comments by Robert Fournier on hydrothermal phenomena and phase changes related to pressure loss were of great value.

May 31, 2000; February 16, 2001

REFERENCES

Allmendinger, R.W., Figueroa, D., Snyder, D., Beer, J., Mpodozis, C., and Isacks, B.L., 1990, Foreland shortening and crustal balancing in the Andes at 30 degrees S latitude: Tectonics, v. 9, p. 789–809.

Arribas, A., Jr., 1995, Characteristics of high-sulfidation epithermal deposits, and their relation to magmatic fluid, *in* Thompson, J.F.H., ed., Magmas, Fluids and Ore Deposits: Mineralogical Association of Canada Short Course Series, v. 23, p. 419–454.

Arribas, A. Jr., Hedenquist, J.W., Itaya, T., Okada, T., Concepcion, R.A., and Garcia, J.S. Jr., 1995, Contemporaneous formation of adjacent porphyry and epithermal Cu-Au deposits over 300 ka in northern Luzon, Philippines: Geology, v. 23, p. 337–340.

Ashley, R.P., and Silberman, M.L., 1976, Direct dating of mineralization at Goldfield, Nevada, by potassium-argon and fission-track methods: Economic Geology, v. 71, p. 904–924.

Bodnar, R.J., 1993, Revised equation and table for determining the freezing point depression of H_2O-NaCl solutions: Geochimica et Cosmochimica Acta, v. 57. p. 683–684.

——1994, Synthetic fluid inclusions. XII. Experimental determinations of the liquidus and isochores for a 40 wt percent H_2O-NaCl solution: Geochimica et Cosmochimica Acta, v. 55. p. 1053–1063.

——1995, Fluid inclusion evidence for a magmatic source for metals in porphyry copper deposits, *in* Thompson, J.F.H., ed., Magmas, Fluids and Ore Deposits: Mineralogical Association of Canada Short Course Series, v. 23, p. 139–152.

Bodnar, R.J., and Vityk, M.O., 1994, Interpretation of microthermometric data for H_2O-NaCl fluid inclusions, *in* De Vivo, B., and Frezotti, M.L., eds., Fluid Inclusions in Minerals: Methods and Applications, Virginia Polytechnic Institute & State University, Blacksburg, Virginia, p. 117–130.

Bodnar, R.J., Burnham, C.W., and Sterner, S.M., 1985, Synthetic fluid inclusions in natural quartz. III. Determination of phase equilibrium properties in the system H_2O-NaCl to 1000°C and 1500 bars: Geochimica et Cosmochimica Acta, v. 49, p. 1871–1873.

Boydell, H.C., 1924, The role of colloidal solutions in the formation of mineral deposits: Transactions of the Institution of Mining and Metallurgy (England), v. 34, p. 145–337.

Brimhall, G.H., Jr., 1979, Lithologic determination of mass transfer mechanisms of multiple-stage porphyry copper mineralization at Butte, Montana: Vein formation by hypogene leaching and enrichment of potassium-silicate protore: Economic Geology, v. 74, p. 556–589.

Brown, A.J., and Rayment, B., 1991, Refugio gold project, Chile: Mining Magazine, v. 165, p. 306–312.

Carten, R.B., Geraghty, E.P., Walker, B.M., and Shannon, J.R., 1988, Cyclic development of igneous features and their relationship to high-temperature hydrothermal features in the Henderson porphyry molybdenum deposit, Colorado: Economic Geology, v. 83, p. 266–296.

Clode, C., Proffett, J.M., Mitchell, P., and Munajat, I., 1999, Relationships of intrusion, wall rock alteration and mineralization in the Batu Hijau copper-gold porphyry deposit: Australasian Institute of Mining and Metallurgy Series 4/99, p. 485–498.

Dalrymple, G.B., Alexander, E.C., Jr., Lanphere, M A., and Kraker, G.P., 1981, Irradiation of samples for $^{40}Ar/^{39}Ar$ dating using the Geological Survey TRIGA Reactor: United States Geological Survey Professional Paper 1176, 55 p.

Davidson, J., and Mpodozis, C., 1991, Regional geologic setting of epithermal gold deposits, Chile: Economic Geology, v. 86, p. 1174–1186.

Deen, J.A., Rye, R.O., Munoz, J.L., and Drexler, J.W., 1994, The magmatic hydrothermal system at Julcani, Peru: Evidence from fluid inclusions and hydrogen and oxygen isotopes: Economic Geology, v. 89, p. 1924–1938.

Dilles, J.H., and Wright, J.E., 1988, The chronology of early Mesozoic arc magmatism in the Yerington district of western Nevada and its regional implications: Geological Society of America Bulletin, v. 100, p. 644–652.

Duffield W.A., and Dalrymple, G.B., 1990, The Taylor Creek Rhyolite of New Mexico: A rapidly emplaced field of lava domes and flows: Bulletin of Volcanology, v. 52, p. 475–487.

Einaudi, M.T., 1977, Environment of ore deposition at Cerro de Pasco, Peru: Economic Geology, v. 72, p. 893–924.

Einaudi, M.T., 1982, Description of skarns associated with porphyry copper plutons, southwestern North America, *in* Titley, S.R., ed., Advances in Geology of the Porphyry Copper Deposits, Southwestern North America: Tucson, University of Arizona Press, p. 139–184.

Flores, R., 1993, Geología del pórfido aurífero Verde, proyecto Refugio, Tercera Región, Chile: Revista Geológica de Chile, v. 20, p. 57–69.

Fournier, R.O., 1985, The behavior of silica in hydrothermal solutions: Reviews in Economic Geology, v. 2, p. 45–60.

——1987, Conceptual models of brine evolution: U.S. Geological Survey Professional Paper 1350, p. 1487–1506.

——1991, The transition from hydrostatic to greater than hydrostatic fluid pressure in presently active continental hydrothermal systems in crystalline rock: Geophysical Research Letters, v. 18, p. 955–958.

——1999, Hydrothermal processes related to movement of fluid from plastic into brittle rock in the magmatic-epithermal environment: Economic Geology, v. 94, p. 1193–1211.

Giletti, B.J., 1974, Studies in diffusion. I. Argon in phlogopite mica, *in* Hoffman, A.W., Giletti, B.J., Yoder, H.S., Jr., and Yund, R.A., eds., Geochemical Transport and Kinetics: Carnegie Institute Washington Publication 634, p. 107–115.

Goldstein, R.H., and Reynolds, T.J., 1994, Systematics of fluid inclusions in diagenetic minerals: SEPM Short Course 31, Society for Sedimentary Geology, 199 p.

Gustafson, L.B., and Hunt, J.P., 1975, The porphyry copper deposit at El Salvador, Chile: Economic Geology, v. 70, p. 857–912.

Gustafson, L.B., Orquera, W., McWilliams, M., Castro, M., Olivarez, O., Rojas, G., Maluenda, J., and Mendez, M., 2001, Multiple centers of mineralization in the Indio Muerto district, El Salvador, Chile: Economic Geology, v. 96. [in press.]

Harrison, T.M., Duncan, I., and McDougall, I., 1985, Diffusion of ^{40}Ar in biotite: Temperature, pressure and compositional effects: Geochimica et Cosmochimica Acta, v. 49, p. 2461–2468.

Heald, P., Foley, N.K., and Hayba, D.O., 1987, Comparative anatomy of volcanic-hosted epithermal deposits: Acid-sulfate and adularia-sericite types: Economic Geology, v. 82, p. 1–26.

Hedenquist, J.W., 1995, The ascent of magmatic fluid: Discharge versus mineralization, *in* Thompson, J.F.H., ed., Magmas, Fluids and Ore Deposits: Mineralogical Association of Canada Short Course Series, v. 23, p. 263–289.

Hedenquist, J.W., Aoki, M., and Shinohara, H., 1994, Flux of volatiles and ore-forming metals from the magmatic-hydrothermal system of Satsuma Iwojima volcano: Geology, v. 22, p. 585–588.

Hedenquist, J.W., Arribas, A., Jr., and Reynolds, T.J., 1998, Evolution of an intrusion-centered hydrothermal system: Far Southeast-Lepanto porphyry and epithermal Cu-Au deposits, Philippines: Economic Geology, v. 93, p. 373–404.

Hedenquist, J.W., Arribas, A., Jr., and Gonzales-Urien, E., 2000, Exploration for epithermal gold deposits: Reviews in Economic Geology, v. 13, p. 245–277.

Heinrich, C.A., Günther, D., Audétat, D., Ulrich, T., and Frischnecht, R., 1999, Metal fractionation between magmatic brine and vapor, determined by microanalysis of fluid inclusions: Geology, v. 27, p. 755–758.

Hemley, J.J., Hostetler, P.B., Gude, A.J., and Mountjoy, W.T., 1969, Some stability relations of alunite: Economic Geology, v. 64, p. 599–612.

Hemley, J.J., and Hunt, J.P., 1992, Hydrothermal ore-forming processes in the light of studies in rock-buffered systems. II. Some general geologic applications: Economic Geology, v. 87, p. 23–43.

Irianto, B., and Clark, G.H., 1995, The Batu Hijau porphyry copper-gold deposit, Sumbawa Island, Indonesia, *in* Mauk, J.L., and St. George, J.D., eds., PACRIM'95 Congress: Australasian Institute of Mining and Metallurgy, Melbourne, 1995, Proceedings, p. 299–304.

Isacks, B.L., 1988, Uplift of the central Andean plateau and bending of the Bolivian orocline: Journal of Geophysical Research, v. 93, p. 3211–3231.

Itaya, T., Arribas, A., Jr., and Okada, T., 1996, Argon release systematics of hypogene and supergene alunite based on progressive heating experiments from 100 to 1000°C: Geochimica et Cosmochimica Acta, v. 60, p. 4525–4535.

John, D.A., 1989, Geologic setting, depths of emplacement, and regional distribution of fluid inclusions in intrusions of the central Wasatch Mountains, Utah: Economic Geology, v. 84, p. 386–409.

Jordan, T.E., Isacks, B.L., Allmendinger, R.W., Brewer, J.A., Ramos, V.A., and Ando, C.J., 1983, Andean tectonics related to geometry of subducted Nazca plate: Geological Society of America Bulletin, v. 94, p. 341–361.

Kay, S.M., Mpodozis, C., Ramos, V.A., and Munizaga, F., 1991, Magma source variations for mid-late Tertiary magmatic rocks associated with a shallowing subduction zone and a thickening crust in the central Andes (28 to 33°S): Geological Society of America Special Paper 265, p. 113–137.

Kay, S.M., Mpodozis, C., Tittler, A., and Cornejo, P., 1994, Tertiary magmatic evolution of the Maricunga mineral belt in Chile: International Geology Reviews, v. 36, p. 1079–1112.

Kesler, S.E., Russell, N., Seaward, M., Rivera, J., McCurdy, K., Cumming, G.L., and Sutter, J.F., 1981, Geology and geochemistry of sulfide mineralization underlying the Pueblo Viejo gold-silver oxide deposit, Dominican Republic: Economic Geology, v. 76, p. 1096–1117.

King, A.R., 1992, Magmatism, structure and mineralization in the Maricunga belt, northern Chile: Unpublished Ph.D. dissertation, London, U.K., Imperial College, 395 p.

Krauskopf, K.B., 1957, The heavy metal content of magmatic vapor at 600°C: Economic Geology, v. 52, p. 786–807.

——1964, The possible role of volatile metal compounds in ore genesis: Economic Geology, v. 59, p. 22–45.

Lanphere, M.A., and Dalrymple, G.B., 1978, The use of $^{40}Ar/^{39}Ar$ data in evaluation of disturbed K-Ar systems: U.S. Geological Survey Open File Report OF 78-701, p. 241–243.

Love, D.A., Clark, A.H., Hodgson, C.J., Mortensen, J.K., Archibald, D.A., and Farrar, E., 1998, The timing of adularia-sericite-type mineralization and alunite-kaolinite-type alteration, Mount Skukum epithermal gold deposit, Yukon Territory, Canada: $^{40}Ar/^{39}Ar$ and U-Pb geochronology: Economic Geology, v. 93, p. 437–462.

Lowell, J.D., and Guilbert, J.M., 1970, Lateral and vertical alteration-mineralization zoning in porphyry copper ore deposits: Economic Geology, v. 65, p. 373–408.

Mancano, D.P., and Campbell, A.R., 1995, Microthermometry of enargite-hosted fluid inclusions from the Lepanto, Philippines, high-sulfidation Cu-Au deposit: Geochimica et Cosmochimica Acta, v. 59, p. 3909–3916.

Marsh, T.M., Einaudi, M.T., and McWilliams, M., 1997, $^{40}Ar/^{39}Ar$ geochronology of Cu-Au and Au-Ag mineralization in the Potrerillos district, Chile: Economic Geology, v. 92, p. 784–806.

McIntyre, G.A., 1963, Precision and resolution in geochronometry, *in* Albritton, C.C., ed., The Fabric of Geology: Reading, Massachusetts, Addison-Wesley Publishing Company, p. 112–134.

McIntyre, G.A., Brooks, C., Compston, W., and Turek, A., 1966, The statistical assessment of Rb-Sr isochrons: Journal of Geophysical Research, v. 71, p. 5459–5468.

Mehnert, H.H., Lipman, P.W., and Steven, T.A., 1973, Age of mineralization at Summitville, Colorado, as indicated by K-Ar dating of alunite: Economic Geology, v. 68, p. 399–412.

Mercado W., M., 1982, Geología de la Hoja Laguna del Negro Francisco, Región de Atacama: Santiago, Servicio Nacional de Geología y Mineréa, Carta Geológica de Chile, no. 56, 73 p.

Meyer, C., and Hemley, J.J., 1967, Wall rock alteration, *in* Barnes, H.L., ed., Geochemistry of Hydrothermal Ore Deposits: New York, Holt Rinehart, and Winston, p. 166–232.

Meyer, C., Shea, E.P., Goddard, C.C., Jr., and Staff, 1968, Ore deposits at Butte, Montana, *in* Ridge, J.D., ed., Ore Deposits of the United States, 1933-67 (Graton-Sales volume): New York, American Institute of Mining, Metallurgy and Petroleum Engineers, v. 2, p. 1373–1416.

Mpodozis, C., Cornejo, P., Kay, S.M., and Tittler, A., 1995, La franja de Maricunga: Sintesis de la evolucion del frente volcanico Oligoceno-Mioceno de la zona sur de los Andes centrales: Revista Geológica de Chile, v. 21, p. 273–313.

Muntean, J.L., 1998, Magmatic-hydrothermal gold deposits of the Maricunga belt, northern Chile: Unpublished Ph.D. dissertation, Stanford, California, Stanford University, 400 p.

Muntean, J.L., and Einaudi, M.T., 2000, Porphyry gold deposits of the Refugio district, Maricunga belt, northern Chile: Economic Geology, v. 95, p. 1445–1472.

Nash, J.T., 1976, Fluid-inclusion petrology: Data from porphyry copper deposits and applications to exploration: U.S. Geological Survey Professional Paper 907D, 16 p.

Onstott, T.C., Hall, C.M., and York, D., 1989, $^{40}Ar/^{39}Ar$ thermochronometry of the Imataca complex, Venezuela: Precambrian Research, v. 42, p. 255–291.

Oviedo, L., Füster, N., Tschischow, N., Ribba, L., Zuccone, A., Grez, E., and Aguilar, A., 1991, General geology of La Coipa precious metal deposit, Atacama, Chile: Economic Geology, v. 86, p. 1287–1300.

Parry, W.T., Wilson, P.N., Jasumback, M., and Heizler, M.T., 1998, Clay mineralogy and $^{40}Ar/^{39}Ar$ dating of phyllic and argillic alteration at Bingham, Utah, *in* John, D.A., and Ballantyne, G.H., eds., Geology and Ore Deposits of the Oquirrh and Wasatch Mountains, Utah: Society of Economic Geologists, Guidebook Series, v. 29, p. 171–188.

Pitzer, K.S., and Pabalan, R.T., 1986, Thermodynamics of NaCl in steam: Geochimica et Cosmochimica Acta, v. 50, p. 1445–1454.

Ramdohr, P., 1980, The ore minerals and their intergrowths—second edition: New York, Pergamon, 1207 p.

Ransome, 1909, Geology and ore deposits of Goldfield, Nevada: U.S. Geological Survey Professional Paper 66, 258 p.

Roedder, E., 1984, Fluid Inclusions, *in* Reviews in Mineralogy, v. 12: Mineralogical Society of America, Washington, D.C., 644 p.

Roedder, E., and Bodnar, R.J., 1980, Geologic pressure determinations from fluid inclusion studies: Annual Review of Earth and Planetary Sciences, v. 8, p. 263–301.

Rye, R.O., 1993, The evolution of magmatic fluids in the epithermal environment: The stable isotope perspective: Economic Geology, v. 88, p. 733–752.

Rye, R.O., Bethke, P.M., and Wasserman, M.D., 1992, The stable isotope geochemistry of acid-sulfate alteration: Economic Geology, v. 87, p. 225–262.

Sander, M.V., and Black, J.E., 1988, Crystallization and recrystallization of growth-zoned quartz crystals from epithermal systems: Implications for fluid inclusion studies: Economic Geology, v. 83, p. 1052–1060.

Saunders, J.A., 1994, Silica and gold textures in bonanza ores of the Sleeper deposit, Humboldt County, Nevada: Evidence for colloids and implications for epithermal ore-forming processes: Economic Geology, v. 89, p. 628–638.

Segerstrom, K., 1968, Geología de las Hojas Copiapó y Ojos del Salado, Provincía de Atacama: Santiago, Chile, Instituto de Investigaciones Geológicas. Boletín 24, 58 p.

Sillitoe, R.H., 1973, The tops and bottoms of porphyry copper deposits: Economic Geology, v. 68, p. 799–815.

——1979, Some thoughts on gold-rich porphyry copper deposits: Mineralium Deposita, v. 14, p. 161–174.

——1983, Enargite-bearing massive sulfide deposits high in porphyry copper systems: Economic Geology, v. 78, p. 348–352.

——1988, Gold and silver in porphyry systems, *in* Schafer, R.N., Cooper, J.J., and Vikre, P.G., eds., Bulk Mineable Precious Metal Deposits of the Western United States: Geological Society of Nevada, Reno, Proceedings, p. 221–231.

——1989, Gold deposits in western Pacific island arcs: The magmatic connection, *in* Keays, R.R., Ramsay, W.R.H., and Groves, D., eds., The Geology of Gold Deposits: The Perspective in 1988: Economic Geology Monograph, v. 6, p. 274–291.

——2000, Gold-rich porphyry deposits: Descriptive and genetic models and their role in exploration and discovery: Reviews in Economic Geology, v. 13, p. 315–345.

Sillitoe, R.H., McKee, E.H., and Vila, T., 1991, Reconnaissance K-Ar geochronology of the Maricunga gold-silver belt, northern Chile: Economic Geology, v. 86, p. 1261–1270.

Souririjan, S., and Kennedy, G.C., 1962, The system H_2O-NaCl at elevated temperatures and pressures: American Journal of Science, v. 260, p. 115–141.

Steiger, R.H., and Jäger, E., 1977, Subcommission on geochronology: Convention on the use of decay constants in geo- and cosmochronology: Earth and Planetary Science Letters, v. 36, p. 359–362.

Taylor, A.V. Jr., 1935, Ore deposits at Chuquicamata, Chile, *in* Copper Resources of the World: International Geological Congress, 16th, Washington, D.C., v. 2, p. 473–484.

Taylor, J.R., 1982, An Introduction to Error Analysis: Mill Valley, California, University Science Books, 269 p.

Vasconcelos, P.M., Brimhall, G.H., Becker, T.A., and Renne, P.R., 1994, $^{40}Ar/^{39}Ar$ analysis of supergene jarosite and alunite: Implications to the paleoweathering history of the western U.S.A. and West Africa: Geochimica et Cosmochimica Acta, v. 59, p. 401–420.

Vila, T., and Sillitoe, R.H., 1991, Gold-rich porphyry systems in the Maricunga belt, northern Chile: Economic Geology, v. 86, p. 1238–1260.

Vila, T., Sillitoe, R.H., Betzhold, J., and Viteri, E., 1991, The porphyry gold deposit at Marte, northern Chile: Economic Geology, v. 86, p. 1271–1286.

Walker, J.A., Moulds, T.N., Zentilli, M., and Feigenson, M.D., 1991, Spatial and temporal variations in volcanics of the Andean central volcanic zone (26 to 28°S): Geological Society of America Special Paper 265, p. 139–155.

Wallace, A.B., 1979, Possible signatures of buried porphyry-copper deposits in middle to late Tertiary volcanic rocks of western Nevada: Nevada Bureau of Mines Report 33, p. 69–75.

Watanabe, Y., Stein, H.J., Morgan, J.W., and Markey, R.J., 1999, Re-Os geochronology brackets the timing and duration of mineralization for the El Salvador porphyry Cu-Mo deposit, Chile [abs.]: Geological Society of America Abstracts with Program, v. 30, p. A-30.

Wright, A.E., and Bowes, D.R., 1963, Classification of volcanic breccias: A discussion: Geological Society of American Bulletin, v. 74, p. 79–86.

Wright, N., Layer, P.W., and York, D., 1991, New insights into thermal history from single grain ^{40}Ar-^{39}Ar analysis of biotite: Earth and Planetary Science Letters, v. 104, p. 70–79.

York, D., 1969, Least squares fitting of a straight line with correlated errors: Earth and Planetary Science Letters, v. 5, p. 320–324.

Zentilli, M., 1974, Geological evolution and metallogenic relationships in the Andes of northern Chile between 26° and 29° south: Unpublished Ph.D. dissertation, Kingston, Ontario, Queen's University, 446 p.

Zweng, P.L., Mortensen, J.K., and Dalrymple, B.G., 1993, Thermochronology of the Campflo gold deposit, Malartic, Quebec: Implications for magmatic underplating and the formation of gold-bearing quartz veins: Economic Geology, v. 88, p. 1700–1721.

APPENDIX
Fluid Inclusions

Fluid inclusion types I, II, and III were recognized using the classification scheme of Nash (1976). Type II inclusions are vapor-rich inclusions. Type I inclusions are liquid-rich inclusions without halite daughter minerals. Type III inclusions are liquid-rich inclusions with halite daughter minerals. Type III inclusions are divided into two subtypes. In type IIIa inclusions halite dissolved before the vapor bubble homogenized, consistent with vapor-saturated conditions, whereas in type IIIb inclusions halite dissolved after the vapor bubble disappeared. Phase equilibrium constraints in the H_2O-NaCl system do not permit type IIIb inclusions to be trapped in equilibrium with a vapor phase (Roedder and Bodnar, 1980; Bodnar, 1994). Nevertheless, ubiquitous and abundant type II inclusions with type IIIb inclusions are strong evidence for immiscible conditions. The formation of type IIIb inclusions is best explained by variable isobaric cooling of the brine to vapor-undersaturated conditions before entrapment (see p. 449–450, Roedder, 1984; John, 1989).

Attempts were made to measure data from fluid inclusion assemblages (see Goldstein and Reynolds, 1994) that contained liquid-dominant (types I or III) and vapor-dominant inclusions (type II). Fluid inclusion assemblages are groups of cogenetic fluid inclusions that were trapped in a growth zone in quartz (primary fluid inclusions) or along a healed fracture (secondary fluid inclusions). The anhedral, granular texture of quartz in A-veinlets precluded the identification of primary fluid inclusion assemblages in growth zones, and fluid inclusion assemblages tied to single secondary fracture planes were not identified. Fluid inclusions occur in seemingly random three-dimensional distributions that most likely represent several populations of secondary fluid inclusion assemblages.

Fluid inclusions from 25 doubly polished plates were described, and microthermometric data were collected from nine samples that included three samples of A-veinlets, five samples of banded quartz veinlets, and one sample of a polymetallic vein. Microthermometric data were collected only from inclusion types I and III using a U.S. Geological Survey gas-flow heating/freezing stage adapted by Fluid Inc. NaCl equivalent salinities were estimated in halite-bearing inclusions by measuring the dissolution temperature of halite and using the equation of Bodnar and Vityk (1994). NaCl equivalent salinities of inclusions without halite were estimated by measuring the melting point of ice and using the equation of Bodnar (1993). Further explanation of methodology, sample descriptions and locations, and individual fluid inclusion measurements, including interpretation of groups of measurements in terms of fluid inclusion assemblages, are found in Muntean (1998).

$^{40}Ar/^{39}Ar$ Analyses

Introduction

Biotite- and alunite-bearing samples were chosen for mineral separation and dating in the context of the time-space frameworks for the three districts. Textural, mineralogic, and paragenetic characteristics of the samples were documented in the laboratory by transmitted and reflected-light petrography, X-ray diffraction, and electron microprobe imagery and analysis.

Attempts to separate sufficient coarse-grained (50–180 μm) muscovite from D-veins and polymetallic veins at Aldebarán and La Pepa were unsuccessful. No attempt was made to date fine-grained sericite or illite because of the relatively poor precision expected from analyzing fine-grained polycrystalline aggregates that could not be purified.

$^{40}Ar/^{39}Ar$ dating of alunite and biotite

Although the reliability of K-Ar dating of alunite is widely accepted and has been confirmed by independent dating of associated hydrothermal and igneous minerals and crosscutting field relations (Mehnert et al., 1973; Gustafson and Hunt, 1975; Ashley and Silberman, 1976; Arribas et al., 1995), there are few published $^{40}Ar/^{39}Ar$ ages for alunite (Kesler et al., 1981; Vasconcelos et al., 1994; Marsh et al., 1997; Love et al., 1998). Love et al. (1998), using Arrhenius-type plots, calculated a closure temperature of 280° ± 20°C for alunite for a cooling rate of 50°C/m.y.

The biotite ages represent cooling ages and not ages of formation. On the basis of experiments and calculations using diffusion parameters, a wide range of blocking temperatures, from 200° to 400°C, have been reported for biotite (e.g., Giletti, 1974; Harrison et al., 1985; Onstott et al., 1989; Wright et al., 1991; Zweng et al., 1993). Blocking temperatures increase with increasing grain size and cooling rate and with decreasing Fe/(Fe + Mg) ratio. The fine grain size of the biotites in this study is probably offset by the low Fe/(Fe + Mg) mole ratios (<0.35, see sample descriptions) and by the high cooling rates associated with the subvolcanic environment compared with batholithic or metamorphic environments. Here we assume a blocking temperature of about 300°C.

The three samples of hydrothermal biotite consist of fine-grained hydrothermal biotite and relict magmatic biotite phenocrysts rimmed by hydrothermal biotite. Fluid inclusion data indicate temperatures well above 300°C and probably between 600° and 700°C for the formation of hydrothermal biotite. Similar Fe/(Fe + Mg) ratios between hydrothermal and relict igneous biotite in the samples from Pancho and Cerro Casale can be used to argue that relict igneous biotite equilibrated chemically with high-temperature hydrothermal fluids. Therefore, if igneous biotite had cooled through its blocking temperature prior to high-temperature alteration, it was completely reset during formation of hydrothermal biotite.

Mineral separation

Minerals were separated by first breaking down the samples to less than a millimeter in grain size and then concentrating biotite or alunite by a variety of magnetic, chemical, and physical processes. The alunite-bearing samples were soaked in a cold 25 percent hydrofluoric acid solution for 1.5 to 5 h to remove silicate and jarosite impurities. Itaya et al. (1996) showed that hydrofluoric acid dissolution for 2 h had no effect on K-Ar ages of alunite on replicate samples. Final

sample selection was done by two stages of hand-picking that took between 10 and 38 hours per sample. Detailed mineral separation procedures are found in Muntean (1998).

$^{40}Ar/^{39}Ar$ analytical method

Mineral separates were individually packaged in 99.99 percent copper foil and placed in a quartz tube for irradiation. Sanidine (85G003) from the 27.92 Ma Taylor Creek Rhyolite, New Mexico (Duffield and Dalrymple, 1990) was placed in similar packets and was used as a neutron flux monitor. Fourteen monitor packets were interspersed with packets of unknown samples, including samples from other studies, throughout the entire quartz tube, and the position of each packet in the tube was carefully measured before and after irradiation. The samples were irradiated for 16 hours in the Oregon State University TRIGA nuclear reactor. After irradiation, one of the alunite samples for which there was ample material (CAV-4 41.5m) was split into two samples for replicate analyses. Argon was extracted and measured at the Stanford University $^{40}Ar/^{39}Ar$ laboratory, which is equipped with an argon-ion laser probe and resistance furnace extraction system; a very low-blank extraction line; and a high-sensitivity, multiple-collector MAP 216 noble-gas mass spectrometer that can measure isotope ratios to ±0.1 percent (1σ). All ages were calculated using the constants recommended by Steiger and Jäger, 1977.

J values were calculated by measuring the isotopic ratios of multiple clusters of two or three sanidine grains from each monitor packet using the laser extraction line. The J values of the unknown samples were estimated by regressing a second-order polynominal curve to the J values calculated from the monitors as a function of position in the quartz tube. The variance of the regression as a function of position in the quartz tube was determined and was used to estimate the uncertainty in J at the position of each unknown sample. Estimated uncertainties in J ranged from 0.11 to 0.13 percent (1σ). The J data and regression curve are presented in Muntean (1998).

After loading, samples were baked in ultrahigh vacuum for 24 h at 250°C, prior to analysis by the mass spectrometer. Samples were analyzed by step-heating in the resistance furnace. At each heating step, the evolved gas was purified by stripping reactive gases with hot Zr-V-Fe and cold Zr-Al getters for 5 min for biotite and 10 min for alunite. Variations in the isotopic ratios of the blank values measured at various temperatures before and after analysis of a sample were considered negligible compared with peak-to-background ratios. Therefore, each sample was assigned a set of blank values that were measured at a single temperature before analysis of the sample.

Corrections were made for atmospheric ^{40}Ar by measuring ^{36}Ar and using the atmospheric $^{40}Ar/^{36}Ar$ ratio of 295.5, unless isotope correlation diagrams suggested another ratio. Corrections were also made for reactor-generated Ar isotopes from K, Ca, and Cl, and for the radioactive decay of ^{37}Ar and ^{39}Ar. Final reduction of data to age spectra and isotope correlation diagrams used the computer program EyeSoreCon, written by Bradley Hacker of the University of California, Santa Barbara, which uses the equations of Dalrymple et al. (1981) to calculate apparent age spectra and uncertainties, and the equations of McIntyre et al. (1966) and York (1969) for the regression of correlated data and the calculation of the mean square of weighted deviates (MSWD) goodness-of-fit statistic.

Results of $^{40}Ar/^{39}Ar$ analyses

Results of the analyses are summarized in Table 4 and Figure 15, and the apparent age spectra are shown in Figure 16. Age plateaus were assessed using the three criteria of Lanphere and Dalrymple (1978): the plateau includes at least three contiguous steps; the plateau constitutes at least 50 percent of the total ^{39}Ar released during the experiment; and steps in the plateau are statistically indistinguishable (concordant) using a 95 percent level of confidence as defined by the critical value test (McIntyre, 1963) without considering the uncertainty in J.

Because of the high precision of isotopic ratio measurements obtained with the modern mass spectrometer at Stanford University, sample steps commonly failed the critical value test. Nevertheless, three of the 10 samples met the criteria for a plateau. Six of the seven remaining samples revealed interpretable plateau-like segments. Ages were calculated as weighted means by weighting the apparent ages in the plateau or plateau-like segment by the inverse of its variance (analytical uncertainty); uncertainties in the weighted means were calculated using error propagation (Taylor, 1982). Uncertainties for all ages are quoted at the 2σ confidence level and include the estimated error in J. In each case, isochron ages are concordant with ages interpreted from the age spectra. Only one isochron failed the MSWD test, and only one sample, on the basis of its isochron, showed evidence for excess argon. Individual isotope correlation diagrams for each sample and the equations used in calculating the weighted means and uncertainties are presented in Muntean (1998).

Sample Descriptions and Locations, (UTM zone 19, Southern Hemisphere)

Hydrothermal biotite from Pancho (Refugio), Sample: LYR-3 45–50 m, UTM coordinates 469089mE, 6954074mN: Biotite from a 5-m interval of drill core that assayed 0.8 ppm Au and 0.1 percent Cu (hypogene) in quartz diorite porphyry cut by A-veinlets and banded quartz veinlets. The separate is a mixture of relict igneous biotite phenocrysts rimmed by hydrothermal biotite and composite grains of fine-grained hydrothermal biotite from veinlets and completely altered hornblende sites. Electron microprobe analyses show Fe/(Fe + Mg) mole ratios of 0.17 to 0.26, with no difference between hydrothermal biotite and relict igneous biotite. Much of the biotite was partially chloritized. A large sample was processed to separate sufficient biotite free of chlorite. The final separate contained biotite grains mostly 75–180 μm in size. Sample amount: 3.12 mg.

Alunite from Pancho (Refugio), Sample: RP030, UTM coordinates 469712mE, 6054360mN: Quartz-alunite ledge exposed in a road cut. Pink patches of bladed alunite up to 300 μm in length. Most of the alunite is 30–200 μm in size. Rare pyrite is seen encapsulated in alunite and quartz. The ledge assayed 96 ppb Au (Table 3). Sample amount: 6.51 mg.

Igneous biotite from Verde West (Refugio), Sample: RV050, UTM coordinates 470085mE, 6953072mN: Biotite phenocrysts from surface exposure of late quartz diorite porphyry

stock located in the center of the Verde West orebody. Biotite is mostly 10 to 30 percent altered to chlorite and clay along grain boundaries and cleavages. Special care was taken to exclude the altered grains during separation. Biotite grains are 180 to 250 μm in size. Sample amount: 1.97 mg.

Igneous biotite from Verde East (Refugio), Sample: RV078, UTM coordinates: 470633mE, 6952804mN: Biotite phenocrysts from surface exposure of late quartz diorite porphyry stock located just west of the Verde East orebody. Two analyses of the biotite show Fe/(Fe + Mg) molar ratios of 0.27 and 0.31. Biotite is mostly 10 to 30 percent altered to chlorite and clay along grain boundaries and cleavages. Special care was taken to exclude the altered grains during separation. Biotite grains are 180 to 250 μm in size. Sample amount: 3.35 mg.

Hydrothermal biotite from Cerro Casale (Aldebarán), Sample: ALC-1 158-159m, UTM coordinates 472501mE, 6926078mN: Biotite from a biotite porphyry dike in drill core within the zone of supergene oxidation. The dike is pervasively altered to hydrothermal biotite + magnetite and is cut by minor, narrow A-veinlets. Core interval assayed 0.46 ppm Au. The biotite porphyry dike truncates A-veinlets at its contact with an earlier intrusion. The separate ranges from 90 to 250 μm in grain size and is a mixture of relict igneous biotite phenocrysts rimmed by hydrothermal biotite and composite grains of fine-grained hydrothermal biotite from veinlets and completely altered hornblende sites. Electron microprobe analyses of relict phenocrysts and hydrothermal biotite have Fe/(Fe + Mg) molar ratios of 0.25 to 0.27 and 0.23, respectively. Sample amount: 4.29 mg.

Alunite from Aldebarán, Sample: AVZ005, UTM coordinates: 471625mE, 6926204mN: Alunite from a ledge about 750 m west-northwest of Cerro Casale. Fault with unknown displacement occurs between the vein and Cerro Casale. The ledge assayed 17 ppb Au (Table 3). Alunite occurs as bladed crystals up to 400 μm in length in altered feldspar phenocryst sites and in veinlets. Sample amount: 12.57 mg.

Hydrothermal biotite from Cavancha (La Pepa), Sample: CAV-2 258-264m, UTM coordinates 476878mE, 6982407mN: Biotite from a feldspar porphyry dike that shows pervasive hydrothermal biotite + magnetite alteration with a minimal chlorite overprint. The sample is from drill core below the zone of supergene oxidation from an interval that assayed 0.48 ppm Au. The separate ranges from 90 to 180 μm in grain size and is a mixture of relict igneous biotite phenocrysts rimmed by hydrothermal biotite and composite grains of fine-grained hydrothermal biotite from veinlets and completely altered hornblende sites. Electron microprobe analyses of the hydrothermal biotite show Fe/(Fe + Mg) molar ratios of 0.34 to 0.35. Sample amount: 2.95 mg.

Alunite from Purpura vein (La Pepa), Sample: LP004W, UTM coordinates 477070mE, 6982715mN: Quartz-alunite ledge cut by gold-bearing enargite-rich chalcedony. Alunite occurs as 25 to 100 μm grains in altered feldspar phenocryst sites and narrow (<0.5 mm) alunite ± pyrite veinlets. Sample amount: 5.84 mg.

Alunite from Liebre vein (La Pepa), Sample: CAV-4 41.5mA,B, UTM coordinates 476762mE, 6982581mN: Quartz-alunite alteration directly adjacent to a zone with erratically developed vuggy quartz from a 2-m drill core interval that assayed 299 ppm Au. The alunite occurs as bladed crystals up to 0.5 mm, locally intergrown with pyrite. Sample amount: 13.52 mg (before irradiation). After the irradiation, the sample was split into two samples, A and B, for replicate analyses.

$^{40}Ar/^{39}Ar$ Data

LYR-3 45-50m, hydrothermal biotite, Pancho deposit, Refugio; J=0.0033156

T (°C)	^{40}Ar (mol)	$^{40}Ar/^{39}Ar$	$^{38}Ar/^{39}Ar$	$^{37}Ar/^{39}Ar$	$^{36}Ar/^{39}Ar$	K/Ca	$\Sigma^{39}Ar$	$^{40}Ar^*$	Age (Ma ± 1σ)
550	1.60E-13	39.8923	4.60E-03	0.3982	0.1269	1.2	0.007	0.060	14.28 ± 0.55
600	7.40E-14	11.9728	3.00E-03	0.2119	0.0271	2.3	0.019	0.332	23.63 ± 0.27
650	9.00E-14	7.6503	1.70E-03	0.1088	0.0124	4.5	0.041	0.522	23.71 ± 0.15
700	1.70E-13	5.8234	1.70E-03	0.0498	0.0062	9.8	0.095	0.683	23.65 ± 0.08
750	2.40E-13	4.8852	1.20E-03	0.0272	0.0031	18	0.183	0.810	23.51 ± 0.04
800	1.90E-13	4.5964	1.40E-03	0.0261	0.0022	19	0.260	0.856	23.39 ± 0.04
850	8.50E-14	4.6950	1.10E-03	0.0673	0.0023	7.3	0.293	0.854	23.82 ± 0.08
900	5.90E-14	4.7954	9.20E-04	0.0990	0.0027	5.0	0.316	0.833	23.72 ± 0.10
950	6.70E-14	4.7929	1.00E-03	0.0880	0.0027	5.6	0.341	0.832	23.70 ± 0.09
1000	1.50E-13	4.5848	6.40E-04	0.0338	0.0020	14	0.402	0.874	23.81 ± 0.04
1050	3.40E-13	4.4369	8.90E-04	0.0198	0.0017	25	0.544	0.884	23.30 ± 0.02
1100	5.50E-13	4.5264	1.20E-03	0.0123	0.0021	40	0.768	0.862	23.17 ± 0.02
1300	5.90E-13	4.6552	1.20E-03	0.0100	0.0025	49	1.000	0.840	23.22 ± 0.02

Total fusion age: 23.31 Ma
Weighted mean age (1,050°–1,300°C; 1,050°C and 1,300°C steps are not concordant): 23.22°0.06 Ma (± 2σ)

RP030, alunite, Pancho deposit, Refugio; J=0.0033011

T (°C)	^{40}Ar (mol)	$^{40}Ar/^{39}Ar$	$^{38}Ar/^{39}Ar$	$^{37}Ar/^{39}Ar$	$^{36}Ar/^{39}Ar$	K/Ca	$\Sigma^{39}Ar$	$^{40}Ar^*$	Age (Ma ± 1σ)
400	3.50E-13	40.7515	5.10E-03	0.4483	0.1257	1.1	0.025	0.088	21.32 ± 0.44
420	1.60E-13	7.4377	0.00E+00	0.1286	0.0121	3.8	0.084	0.517	22.78 ± 0.07
440	3.10E-13	5.636	0.00E+00	0.0831	0.0062	5.9	0.241	0.675	22.51 ± 0.03
460	5.40E-13	4.9614	0.00E+00	0.0714	0.0038	6.9	0.548	0.777	22.80 ± 0.03
480	7.10E-13	5.4073	0.00E+00	0.1076	0.0055	4.6	0.921	0.699	22.35 ± 0.02
500	1.50E-13	6.1236	6.10E-04	0.3297	0.0081	1.5	0.991	0.608	22.04 ± 0.05
600	4.20E-14	12.4525	3.50E-03	1.6808	0.0302	0.29	1.000	0.284	20.95 ± 0.26

Total fusion age: 22.48 Ma

RV050, igneous biotite, Verde deposit, Refugio; J=0.0032866

T (°C)	^{40}Ar (mol)	$^{40}Ar/^{39}Ar$	$^{38}Ar/^{39}Ar$	$^{37}Ar/^{39}Ar$	$^{36}Ar/^{39}Ar$	K/Ca	$\Sigma^{39}Ar$	$^{40}Ar^*$	Age (Ma ± 1σ)
550	8.40E-14	55.9821	8.70E-03	0.6395	0.1766	0.77	0.004	0.068	22.28 ± 1.29
600	2.60E-14	20.2039	6.40E-03	0.6783	0.0559	0.72	0.008	0.183	21.75 ± 0.97
650	2.50E-14	9.1235	5.50E-03	0.3775	0.0171	1.3	0.016	0.446	23.93 ± 0.43
700	3.20E-14	5.5831	4.30E-03	0.1733	0.0068	2.8	0.033	0.638	20.97 ± 0.30
750	5.60E-14	5.0421	1.30E-03	0.0780	0.0039	6.3	0.066	0.774	22.98 ± 0.12
800	9.60E-14	4.5130	9.00E-04	0.0183	0.0019	27	0.128	0.878	23.34 ± 0.06
850	1.40E-13	4.2861	1.30E-03	0.0245	0.0011	20	0.224	0.925	23.35 ± 0.04
900	1.80E-13	4.1834	1.10E-03	0.0261	0.0008	19	0.347	0.942	23.22 ± 0.14
950	1.70E-13	4.1319	1.20E-03	0.0251	0.0006	20	0.466	0.955	23.24 ± 0.03
1000	1.30E-13	4.1702	1.00E-03	0.0134	0.0007	37	0.555	0.947	23.27 ± 0.04
1050	1.20E-13	4.5349	1.20E-03	0.0162	0.0019	30	0.634	0.877	23.42 ± 0.09
1100	9.00E-14	4.5099	1.10E-03	0.0303	0.0019	16	0.693	0.878	23.31 ± 0.07
1300	4.50E-13	4.2996	1.10E-03	0.0065	0.0012	76	1.000	0.919	23.28 ± 0.02

Total fusion age: 23.24 Ma
Weighted mean plateau age (900°–1300°C): 23.27 ± 0.06 Ma (± 2σ)

RV078, igneous biotite, Verde deposit, Refugio; J=0.0032704

T (°C)	^{40}Ar (mol)	^{40}Ar/^{39}Ar	^{38}Ar/^{39}Ar	^{37}Ar/^{39}Ar	^{36}Ar/^{39}Ar	K/Ca	Σ^{39}Ar	^{40}Ar*	Age (Ma ± 1σ)
550	9.50E-14	43.4773	6.60E-03	0.5260	0.1388	0.93	0.004	0.057	14.44 ± 0.78
600	4.00E-14	19.7831	5.10E-03	0.6216	0.0550	0.79	0.007	0.178	20.66 ± 0.71
650	7.70E-14	12.8060	2.60E-03	0.2014	0.0301	2.4	0.018	0.306	22.93 ± 0.29
700	1.50E-13	8.0907	1.10E-03	0.0659	0.0138	7.4	0.05	0.496	23.52 ± 0.10
750	2.00E-13	5.2105	1.50E-03	0.0329	0.0039	15	0.117	0.778	23.74 ± 0.06
800	1.60E-13	4.7817	8.60E-04	0.0346	0.0025	14	0.175	0.845	23.69 ± 0.05
850	1.30E-13	4.5829	9.90E-04	0.0331	0.0018	15	0.223	0.886	23.79 ± 0.05
900	1.00E-13	4.6008	6.40E-04	0.0421	0.0019	12	0.261	0.879	23.69 ± 0.06
950	1.10E-13	4.5063	8.70E-04	0.0425	0.0017	12	0.303	0.891	23.52 ± 0.05
1000	1.70E-13	4.2947	5.20E-04	0.0200	0.0009	24	0.372	0.939	23.63 ± 0.04
1050	3.30E-13	4.1295	6.90E-04	0.0172	0.0005	28	0.511	0.964	23.33 ± 0.02
1100	8.20E-13	4.1173	6.20E-04	0.0086	0.0005	57	0.855	0.964	23.26 ± 0.01
1300	3.50E-13	4.1663	7.60E-04	0.0153	0.0007	32	1.000	0.953	23.28 ± 0.02

Total fusion age: 23.37 Ma
Weighted mean age (1,050°–1,300°C, 1,050° and 1,100° are not concordant): 23.28 ± 0.06 Ma (± 2σ)

ALC-1 158-159m, hydrothermal biotite, Casale Hill deposit, Aldebarán, J=0.0033457

T (°C)	^{40}Ar (mol)	^{40}Ar/^{39}Ar	^{38}Ar/^{39}Ar	^{37}Ar/^{39}Ar	^{36}Ar/^{39}Ar	K/Ca	Σ^{39}Ar	^{40}Ar*	Age (Ma ± 1σ)
550	2.40E-13	20.3725	8.90E-03	0.2838	0.0664	1.7	0.013	0.020	2.51 ± 317
600	1.90E-13	9.7594	2.70E-03	0.1075	0.0265	4.6	0.035	0.151	8.89 ± 0.13
650	2.40E-13	5.9154	1.50E-03	0.0405	0.0123	12	0.081	0.348	12.37 ± 0.07
700	3.10E-13	3.6888	1.30E-03	0.0232	0.0047	21	0.175	0.602	13.35 ± 0.04
750	2.90E-13	2.9295	1.20E-03	0.0142	0.0020	34	0.285	0.786	13.84 ± 0.02
800	1.90E-13	3.6541	1.60E-03	0.0217	0.0044	23	0.344	0.622	13.67 ± 0.05
850	1.20E-13	3.7030	1.30E-03	0.0410	0.0045	12	0.380	0.619	13.77 ± 0.06
900	9.30E-14	3.8055	1.50E-03	0.0504	0.0048	9.7	0.407	0.607	13.89 ± 0.07
950	1.70E-13	4.0704	1.30E-03	0.0300	0.0056	16	0.453	0.566	13.85 ± 0.05
1000	2.30E-13	3.5403	1.20E-03	0.0164	0.0039	30	0.524	0.654	13.91 ± 0.03
1050	3.10E-13	2.8340	1.00E-03	0.0112	0.0017	44	0.645	0.815	13.89 ± 0.02
1100	5.30E-13	2.5405	1.10E-03	0.0054	0.0007	91	0.879	0.910	13.90 ± 0.01
1300	2.70E-13	2.5401	1.00E-03	0.0110	0.0007	45	1.000	0.908	13.86 ± 0.02

Total fusion age: 13.42 Ma
Weighted mean plateau age (900°–1,300°C): 13.89 ± 0.04 Ma (± 2σ)

AVZ005, alunite, Vein zone, Aldebarán, J=0.0033861

T (°C)	^{40}Ar (mol)	^{40}Ar/^{39}Ar	^{38}Ar/^{39}Ar	^{37}Ar/^{39}Ar	^{36}Ar/^{39}Ar	K/Ca	Σ^{39}Ar	^{40}Ar*	Age (Ma ± 1σ)
400	5.00E-13	19.135	2.10E-03	0.2258	0.0575	2.2	0.047	0.112	13.06 ± 0.15
420	2.80E-13	5.0266	0.00E+00	0.0937	0.0093	5.2	0.146	0.452	13.81 ± 0.04
440	4.30E-13	3.7543	0.00E+00	0.0633	0.0050	7.7	0.353	0.607	13.87 ± 0.02
460	5.60E-13	3.4695	0.00E+00	0.0468	0.0040	10	0.641	0.658	13.90 ± 0.02
480	5.80E-13	3.0762	0.00E+00	0.0632	0.0027	7.8	0.980	0.745	13.94 ± 0.01
500	4.00E-14	4.2362	6.30E-04	0.5909	0.0068	0.83	0.997	0.525	13.52 ± 0.08
600	2.10E-14	11.067	4.70E-03	2.2277	0.0299	0.22	1.000	0.201	13.53 ± 0.42

Total fusion age: 13.85 Ma
Weighted mean age (420°–480°C; 480° is not concordant with 420° and 440°): 13.91 ± 0.04 Ma (± 2σ)

CAV-2 258-264m, hydrothermal biotite, Cavancha deposit, La Pepa; J=0.0032392

T (°C)	^{40}Ar (mol)	^{40}Ar/^{39}Ar	^{38}Ar/^{39}Ar	^{37}Ar/^{39}Ar	^{36}Ar/^{39}Ar	K/Ca	Σ^{39}Ar	^{40}Ar*	Age (Ma ± 1σ)
550	1.10E-13	36.4125	2.20E-03	0.1061	0.1125	4.6	0.014	0.087	18.38 ± 0.66
600	6.70E-14	12.0166	3.30E-03	0.0183	0.0273	27	0.041	0.329	22.91 ± 0.32
650	1.30E-13	8.4353	1.80E-03	0.0050	0.0148	98	0.115	0.482	23.61 ± 0.14
700	2.10E-13	5.8407	1.70E-03	0.0013	0.0060	372	0.288	0.699	23.68 ± 0.06
750	2.20E-13	4.8682	1.80E-03	0.0047	0.0026	104	0.505	0.845	23.87 ± 0.04
800	1.30E-13	4.8607	1.60E-03	0.0040	0.0026	123	0.634	0.843	23.78 ± 0.06
850	9.70E-14	4.9366	2.00E-03	0.0141	0.0028	35	0.727	0.831	23.82 ± 0.07
900	6.90E-14	5.2552	1.60E-03	0.0130	0.0041	38	0.789	0.767	23.40 ± 0.11
950	7.30E-14	5.4050	1.40E-03	0.0162	0.0046	30	0.853	0.747	23.43 ± 0.11
1000	1.50E-13	4.9026	1.60E-03	0.0043	0.0027	115	1.000	0.836	23.80 ± 0.05

Total fusion age: 23.63 Ma
Weighted mean age (650°–850°C, 700° and 750° are not concordant): 23.81±0.08 Ma (±2σ)

LP004W, alunite, Purpura vein, La Pepa, J=0.0033315

T (°C)	^{40}Ar (mol)	^{40}Ar/^{39}Ar	^{38}Ar/^{39}Ar	^{37}Ar/^{39}Ar	^{36}Ar/^{39}Ar	K/Ca	Σ^{39}Ar	^{40}Ar*	Age (Ma ± 1σ)
400	4.50E-13	13.0321	4.40E-04	0.1105	0.0323	4.4	0.068	0.268	20.86 ± 0.10
420	4.00E-13	4.6293	0.00E+00	0.0668	0.0027	7.3	0.236	0.829	22.92 ± 0.02
440	9.20E-13	4.1766	0.00E+00	0.0478	0.0008	10	0.663	0.943	23.51 ± 0.01
450	4.70E-13	4.1535	0.00E+00	0.1133	0.0007	4.3	0.881	0.947	23.50 ± 0.03
460	2.10E-13	4.2333	1.60E-04	0.2666	0.0012	1.8	0.979	0.920	23.25 ± 0.02
480	4.30E-14	4.6371	2.50E-03	1.1747	0.0036	0.42	0.997	0.769	21.30 ± 0.07
600	2.00E-14	15.4531	1.50E-02	7.0789	0.0463	0.069	1.000	0.115	10.63 ± 0.59

Total fusion age: 23.13 Ma
Weighted mean age (440°–450°C, only 2 steps): 23.50 ± 0.06 Ma (± 2σ)

CAV-4 41.5mA, alunite, Liebre Vein, La Pepa, J=0.0032557

T (°C)	^{40}Ar (mol)	^{40}Ar/^{39}Ar	^{38}Ar/^{39}Ar	^{37}Ar/^{39}Ar	^{36}Ar/^{39}Ar	K/Ca	Σ^{39}Ar	^{40}Ar*	Age (Ma ± 1σ)
450	1.70E-12	12.3674	0.00E+00	0.0368	0.0282	13	0.608	0.325	23.47 ± 0.06
500	8.70E-13	10.0474	0.00E+00	0.0464	0.0206	11	0.987	0.393	23.03 ± 0.07
550	7.40E-14	30.6786	2.80E-03	0.8940	0.0896	0.55	0.998	0.137	24.56 ± 0.50
575	4.50E-15	16.7555	1.60E-02	7.7756	0.0440	0.063	0.999	0.223	21.78 ± 2.25
600	2.50E-15	11.1181	7.70E-03	6.9161	0.0241	0.071	1.000	0.359	23.25 ± 2.83

Total fusion age: 23.31 Ma
Weighted mean age (450°C, only 1 step): 23.47 ± 0.12 Ma (± 2σ)

CAV-4 41.5mB (replicate analysis), alunite, Liebre Vein, La Pepa, J=0.0032557

T (°C)	^{40}Ar (mol)	^{40}Ar/^{39}Ar	^{38}Ar/^{39}Ar	^{37}Ar/^{39}Ar	^{36}Ar/^{39}Ar	K/Ca	Σ^{39}Ar	^{40}Ar*	Age (Ma ± 1σ)
400	2.40E-13	24.4374	3.70E-03	0.5672	0.0697	0.86	0.020	0.157	22.44 ± 0.31
420	6.00E-13	15.113	0.00E+00	0.1515	0.0377	3.2	0.098	0.263	23.23 ± 0.10
440	1.30E-12	13.5137	0.00E+00	0.0722	0.0322	6.8	0.294	0.295	23.26 ± 0.08
460	1.60E-12	7.9590	0.00E+00	0.0576	0.0134	8.5	0.700	0.501	23.25 ± 0.03
480	1.20E-12	8.7185	0.00E+00	0.0728	0.0162	6.7	0.971	0.451	22.96 ± 0.06
500	2.40E-13	18.9187	1.30E-03	0.5175	0.0502	0.95	0.996	0.216	23.83 ± 0.17
525	6.00E-14	48.1758	8.40E-03	3.9343	0.1477	0.12	0.998	0.094	26.40 ± 1.04
600	2.30E-14	24.1155	8.60E-03	4.2692	0.0663	0.11	1.000	0.187	26.30 ± 0.79

Total fusion age: 23.18 Ma
Weighted mean plateau age (420°–460°C): 23.25 ± 0.08 Ma (± 2σ)